Lawrence Berkeley National Laboratory
Lawrence Berkeley National Laboratory

Title
ELECTROSTATIC PROBE DIAGNOSTICS ON THE LBL 10 AMPERE NEUTRAL BEAM ION SOURCE

Permalink
https://escholarship.org/uc/item/2gc314ww

Author
Schoenberg, Kurt F.

Publication Date
1978-08-01

eScholarship.org Powered by the California Digital Library
University of California

ELECTROSTATIC PROBE DIAGNOSTICS ON THE LBL 10 AMPERE NEUTRAL BEAM ION SOURCE

August 1978

Kurt F. Schoenberg
Lawrence Berkeley Laboratory
University of California
Berkeley, California

NOTICE

This report was prepared as an account of work sponsored by the United States Government. Neither the United States nor the United States Department of Energy, nor any of their employees, nor any of their contractors, subcontractors, or their employees, makes any warranty, express or implied, or assumes any legal liability or responsibility for the accuracy, completeness or usefulness of any information, apparatus, product or process disclosed, or represents that its use would not infringe privately owned rights.

THIS DOCUMENT IS UNLIMITED

TABLE OF CONTENTS

ELECTROSTATIC PROBE DIAGNOSTICS ON THE LBL 10 AMPERE NEUTRAL BEAM ION SOURCE

Kurt F. Schoenberg

Lawrence Berkeley Laboratory
University of California
Berkeley, CA 94720

ABSTRACT

The experimental results of electrostatic probe measurements on the LBL 10 ampere ion source are presented. Data is obtained via a pulsed acquisition system which digitally records a probe characteristic and its first and second derivatives. The latter are shown to be proportional to the projected electron energy distribution function, and the isotropic electron energy distribution function, respectively. System performance for distribution function measurement is compared to the established technique of harmonic analysis. A complete analysis of the data acquisition system and its experimental accuracy is presented.

Experimental measurements include the electron energy distribution function $f_e(\vec{r},\epsilon)$, and variation of general plasma properties (bulk electron temperature, plasma potential, plasma density, saturated ion current, arc discharge current and anode potential) as a function of source spatial position, arc power and input gas flow. The results are compared to previous experimental work and prevailing theories where feasible.

INTRODUCTION

This paper presents the experimental technique and results of electrostatic probe measurements performed on the Lawrence Berkeley Laboratory 10 ampere neutral beam ion source. Experimentally, the Berkeley source is well suited for probe measurements due to several considerations:

1. The plasma chamber is relatively compact and thus general diagnostic access is limited without substantial source modification.
2. The plasma's transient nature and associated low frequency noise characteristics require a diagnostic capable of high speed data acquisition in order to minimize experimental measurement error.
3. The short Debye length encountered in the source greatly simplifies probe data analysis, while allowing for local plasma measurements.

The motivation for probe measurements, as with any diagnostic, is to provide experimental input to theoretical models describing source operation. In particular, measurement of the electron energy distribution function, $f_e(\vec{r},\varepsilon)$, is necessary to predict parameters such as plasma potential distribution, plasma density, loss and ionization rates, etc. which characterize the arc discharge. Measurement of general plasma parameters as a function of source operating conditions, is required to self-consistently check such predictions. A better understanding of these parameters, and the physics governing their behavior, will hopefully lend guidance for improving source performance.

THE 10 AMPERE SOURCE

The 10 ampere source is basically a small version of the hot cathode ion sources presently employed in the Lawrence Berkeley Laboratory neutral beam program.[1] A cross sectional schematic and photograph are shown in Figs. 1A and 1B respectively. The source produces a plasma via a diffuse, low pressure, high current electrical discharge. Arc ionization is produced by primary electrons originating at the thermionic cathode (filament ring), and energized by their passage through the cathode-plasma sheath. The arc discharge occurs between the filament ring, consisting of 26 hairpin tungsten filaments connected in parallel, and the anode ring. A pulse line composed of iron core inductors and electrolytic capacitors, supplies roughly 10 to 60 kW of arc power for up to 100 msec. All source chamber walls electrically float at potentials such that the net random current due to electron and ion bombardment is nulled. The main volume of the discharge is relatively magnetic field free, although both filament heater current and arc discharge current contribute to a field in the vicinity of the filaments. For this reason, the applied filament current is D.C. to minimize A.C. modulation of discharge conditions. To avoid formation of a substantial anode sheath, which increases discharge noise, anode area is chosen such that the discharge arc current is supplied by the random electron flux striking the anode.

Experimental access to the plasma is via two radial probe ports near the source midplane, one radial probe port near the floating extractor grid, one axial probe port, and a section of axially symmetric floating wall which can be used as an extended wall probe.

THEORY OF MEASUREMENT

The Berkeley source operates in a regime where cylindrical or spherical probe operating conditions are adquately described by the collisionless thin sheath approximation, i.e.,

$$\bar{\lambda} \gg r_p \gg \lambda_D \text{ where } \bar{\lambda} \equiv \text{Collisional Mean Free Path} \sim \frac{18\pi n_e \lambda_D^4}{\ln(12\pi n \lambda_D^3)}$$

$$\lambda_D \equiv \text{Electron Debye Length} = \sqrt{kT_e/4\pi n_e e^2}$$

$$r_p \equiv \text{Probe radius}$$

A schematic typical of a probe current-voltage characteristic in this regime is shown in Fig. 2. The experimentally important quantities are:

1. Accurate determination of the Plasma Potential V_p.
2. Accurate determination of the Probe Floating Potential V_f.
3. Accurate measurement of the ion-saturation region (A).
4. Accurate measurement of the electron-transition region (B).

For the case where the electron temperature far exceeds the ion temperature, collected ion current density is quite insensitive to ion temperature and is expressed as

$$j_i(V_\phi) = \left(\frac{1}{4} n_i Z_i e \sqrt{\frac{8kT_e}{\pi m_i}}\right) i_+ (V_\phi; T_e, T_i, r_p, \lambda_D) \qquad (1)$$

where i_+ is an ion current correction factor computed by the theory of Laframboise,[2] and V_ϕ is the probe bias voltage measured with respect to the plasma potential, i.e. $V_\phi = V_p - V$.

The electron current density in the transition region can be expressed in terms of the isotropic electron velocity distribution function $f_e(v)$, as

$$j_e(V_\phi) = n_e e\langle v\rangle(V_\phi) = e\int_{\sqrt{\frac{2eV_\phi}{m_e}}}^{\infty} v^3 f_e(v) \int_{\frac{1}{v}\sqrt{\frac{2eV_\phi}{m_e}}}^{1} \cos\theta\, d(\cos\theta) \int_0^{2\pi} d\phi \tag{2}$$

Performing the angle integration yields

$$j_e(V_\phi) = \pi e\int_{\sqrt{\frac{2eV_\phi}{m_e}}}^{\infty} v^3 f_e(v)\left(1 - \frac{2eV_\phi}{m_e v^2}\right) dv \tag{3}$$

Considering that electron current density is experimentally measured as a function of bias potential, a more convenient description of $j_e(V_\phi)$ is obtained by expressing it as a function of $f_e(\varepsilon)$, the isotropic electron energy distribution function. Defining $f_e(\varepsilon)$ as

$$f_e(\varepsilon) = \int_0^{\infty} f_e(v)\delta(\varepsilon - \tfrac{1}{2} m_e v^2) dv \tag{4}$$

equation (3) becomes

$$j_e(V_\phi) = \frac{2\pi e}{m_e^2}\int_{eV_\phi}^{\infty} \varepsilon\, f_e(\varepsilon)\left(1 - \frac{eV_\phi}{\varepsilon}\right) d\varepsilon \tag{5}$$

For the special case of a Maxwellian Plasma,

$$f_e(\varepsilon) = n_e\left(\frac{m_e}{2\pi kT_e}\right)^{3/2} e^{-\varepsilon/kT_e} \tag{6}$$

which when substituted into equation (5), yields the familiar result

$$j_e(V_\phi) = \frac{1}{4} n_e e \sqrt{\frac{8kT_e}{\pi m_e}} \; e^{-eV_\phi/kT_e} \tag{7}$$

where the electron temperature is given by the inverse slope of $\ln j_e(V_\phi)$ vs V_ϕ. For the general case where $f_e(\varepsilon)$ deviates from a Maxwellian, the electron current density will behave according to equation (5). The fact that $j_e(V_\phi)$ is related to $f_e(\varepsilon)$ through an integral equation, coupled with experimental measurement uncertainties, makes it quite insensitive to all but gross distribution function structure. Finer grained resolution is possible by performing the first and second derivatives of $j_e(V_\phi)$. Taking the second derivative with respect to bias voltage of equation (5) yields

$$\frac{d^2 j_e(V_\phi)}{dV_\phi^2} = \frac{d}{dV_\phi}\left(\frac{2\pi e}{m_e^2}\int_{eV_\phi}^{\infty} \frac{\partial}{\partial V_\phi}\, \varepsilon f_e(\varepsilon)\left(1 - \frac{eV_\phi}{\varepsilon}\right) d\varepsilon\right) = \frac{2\pi e^3}{m_e^2} f_e(V_\phi) \tag{8}$$

Hence,

$$f_e(\varepsilon) = \frac{m_e^2}{2\pi e^3} \left.\frac{d^2 j_e(V_\phi)}{dV_\phi^2}\right|_{eV_\phi = \varepsilon} \tag{9}$$

which relates the electron energy distribution function to the second derivative of the electron probe current density[3,4]*

A further generalization for anisotropic distribution functions is possible by defining $f_e(u,\hat{n})$, the projected electron velocity

*The above treatment required $f_e(\varepsilon)$ to be isotropic. However, the applicability of equation (9) to anisotropic distribution functions, may also be quasi-valid under certain restrictive conditions for spherical probes.[4,5]

distribution function in the spatial direction $\hat{n}$, as

$$f_e(u,\hat{n}) = \int_{\text{all } \vec{v}} d\vec{v}\, f_e(\vec{v})\,\delta(\hat{n}\cdot\vec{v} - u) \tag{10}$$

where $f_e(\vec{v})$ is the general electron velocity distribution function. In terms of $f_e(u,\hat{n})$, equation (2) reduces to

$$j_e(V_\phi) = e \int_{\sqrt{\frac{2eV_\phi}{m_e}}}^{\infty} f_e(u,\hat{n})\, u\, du \tag{11}$$

where $\hat{n}$ now refers to the spatial direction normal to the probe surface. Again, defining $f_e(\varepsilon,\hat{n})$, the projected electron energy distribution function as

$$f_e(\varepsilon,\hat{n}) = \int_0^{\infty} f_e(u,\hat{n})\,\delta(\varepsilon - \tfrac{1}{2} m u^2)\, du \tag{12}$$

equation (11) becomes

$$j_e(V_\phi) = \frac{e}{m_e} \int_{eV_\phi}^{\infty} f_e(\varepsilon,\hat{n})\, d\varepsilon \tag{13}$$

Performing the first derivative with respect to bias voltage yields

$$\frac{dj_e(V_\phi)}{dV_\phi} = -\frac{e^2}{m_e} f_e(V_\phi,\hat{n}) \tag{14}$$

or

$$f_e(\varepsilon,\hat{n}) = -\frac{m_e}{e^2} \left.\frac{dj_e(V_\phi)}{dV_\phi}\right|_{eV_\phi = \varepsilon} \tag{15}$$

When used with a judiciously designed plane or wall probe, equation (15) affords a convenient method of measuring the projected distribution function in any spatial direction.

EXPERIMENTAL APPARATUS

All probe characteristic measurements and the vast majority of all electron distribution function measurements were made using a pulsed data acquisition system, which digitally records the probe characteristic and its first and second derivatives. Several distribution function measurements employed the second harmonic or intermodulation technique, which uses the nonlinearity of the probe current-voltage chracteristic to obtain its second derivative. This technique was primarily employed as an auxiliary check on the reliability and accuracy of the pulsed acquisition system. A complete description and accuracy analysis of the two techniques are given below. A photograph of the overall apparatus is shown in Fig. 3.

I. Pulsed Probe Data Acquisition System

The motivation for a pulsed detection system, in addition to the plasma's transient nature, is readily apparent from its noise spectrum (Fig. 4). The large noise increase below 1 kHz is presumably due to power supply effects. Data acquisition in a time less than 1 ms is necessary to minimize this noise influence.

Figure 5 schematically illustrates the probe driver/detection circuit. An initial pulse, obtained from the source logic, operates the timing of various source inputs. (e.g. application of arc power, filament power, gas injection, etc.) The pulse is also applied to a variable delay gate (enabling data acquisition at any subsequent moment during source operation), amplified, and then used to trigger the probe driver and data recording system. The probe driver initially

applies a large positive bias to the probe to insure a clean collection surface, followed by a linearly decreasing voltage ramp which sweeps the probe bias over its entire operating range. Sweep speeds of .1 v/μsec to 1 v/μsec over a total range of 100 volts are typical. The probe current is differentially detected across a standard resistance and then processed by the differentiation network, which outputs the probe current and its first and second derivatives. These signals are digitally recorded by a Nicolet transient digitizer, which simultaneously samples the processed current signal and its corresponding bias voltage. The stored data is accessible both graphically and as a digitized set of data points; each point consisting of two, twelve bit words (e.g., (V,i) for probe characteristic measurements) with a maximum of 2048 points per data set. The digitized data is finally read by a Modcomp Systems computer via a direct I/O link, which subsequently executes an analysis algorithm providing on line data analysis.

Over all conditions encountered in the Berkeley source, a single data set is sufficient to accurately determine all important experimental quantities obtainable from the probe characteristic or its first derivative. Typical times for complete data acquisition range from .1 ms to 1 ms. However, the comparatively large effective noise bandwith inherent in the operation of a differentiation network, ofttimes requires an ensemble type average over multiple data sets for second derivative measurements, in order to minimize ambient noise effects and increase measurement resolution. For transient plasmas, this technique requires a good shot to shot reproducibility in the plasma's operating conditions. The Berkeley source is found to satisfy this requirement.

In general, accurate temporal differentiation by an electronic network, requires the network frequency response function, $D(\omega)$, be directly proportional to ω. This is easily seen by noting that the Fourier Transform of the time derivative operator (d/dt), is $(-i\omega)$. Using the standard definition of dB voltage gain per octave,

$$G_{oct} \equiv \left\{ \begin{array}{c} \text{Voltage gain} \\ \text{per octave in} \\ \text{dB} \end{array} \right\} = 20 \log_{10} \left| \frac{D(2\omega)}{D(\omega)} \right| \qquad (16)$$

a time derivative network will have a gain per octave of

$$G_{oct} = 20 \log_{10}(2) \sim 6 \text{ dB} \qquad (17)$$

The differentiation network illustrated in Fig. 6A, consists of a series of ganged stages, each stage tailored to a particular frequency response which minimizes overall network noise and instability, while maintaining differentiation accuracy over a 100 kHz bandwidth. All stages utilize compensated AD 507 wideband, low noise operational amplifiers, which have proven quite cost effective. Components for the differentiation stages (Fig. 6B) were chosen to insure a 6 dB/octave gain increase over a 100 kHz bandwidth and stability over all operating conditions. Buffer stages are low pass butterworth filters with flat pass bands from 0-100 kHz.

II. Accuracy Analysis of the Pulsed Acquisition System

The accuracy of the data acquisition process is dependent on the response characteristic of the probe driver circuit, the acquisition accuracy of the probe current detection network, and the temporal linearity of the probe bias voltage ($V_\phi \propto t$); which enables a direct

connection between the time derivatives performed by the differentiation network, and the derivatives with respect to voltage shown proportional to distribution functions (Equations 9 and 15).

A circuit equivalent model of the probe/driver is illustrated in Fig. 7. A discrete circuit model should remain a reasonable approximation for response times slow compared to an ion plasma period. The temporal response of the circuit model is roughly

$$\tau_{system} = \frac{R_D R_S (C_D + C_S)}{(R_D + R_S)} \tag{18}$$

where $C_D(R_D)$ are the effective driver circuit capacitance (resistance) and $C_S(R_S)$ are the effective probe-plasma sheath capacitance (resistance) respectively. For realistic experimental systems, $C_S << C_D$,[6] and R_D can usually be made much smaller than R_S through judicial driver circuit and probe design. Therefore, the probe driver electronics completely determines the temporal response of the system. The measured frequency response of the driver section depicted in Fig. 7, was linear over a 100-kHz bandwidth, with a loaded slew rate of 10 V/μsec.

Since the probe current detection network operates on time dependent probe current, network acquisition accuracy is strongly dependent on its temporal response. The spectral density of the probe current density j(t), is given by its Fourier Transform

$$J(\omega) = \int_{-\infty}^{\infty} j(t)\, e^{-i\omega t}\, dt \tag{19}$$

Given $D(\omega)$, the network respose function of the detection system, the detected current density is*

$$j_{DET}(t) = \frac{1}{2\pi}\int_{-\infty}^{\infty} D(\omega)\ J(\omega)\ e^{i\omega t}d\omega = \int_{-\infty}^{t} d(t-\tau)j(\tau)d\tau \qquad (20)$$

where $d(t-\tau)$, the Network Transfer Function, is given by

$$d(t-\tau) = \frac{1}{2\pi}\int_{-\infty}^{\infty} D(\omega)\ e^{i\omega(t-\tau)}d\omega \qquad (21)$$

A rather exact form of $D(\omega)$ is obtainable from amplitude and phase response measurements for each of the network functions of interest, although an analytic solution of equation (21) is practically unobtainable. Numerical solutions of equations (21) and (20) are possible, albeit somewhat tedious.[11,12] For estimation purposes, a qualitative solution of equation (21) is possible by noting that since all network functions perform effectively over a 100-kHz bandwidth, the analysis of network accuracy reduces to finding the effect of a finite bandwidth response on the detected signal. This amplitude response can be modeled by the step function

$$\begin{aligned} |D(\omega)| &= 1 \qquad 0 \le |\omega| \le \omega_c \\ &= 0 \qquad |\omega| > \omega_c \end{aligned} \qquad (22)$$

*In general, the causal behavior of equation (20) requires $D(\omega)$ be a complex function whose real and imaginary parts, describing network amplitude and phase response, are related via the Kramers-Kronig relations?[7]

where ω_c is the angular high frequency cut-off. Substituting in equation (21) yields

$$d(t-\tau) = \frac{\omega_c}{\pi} \text{Sinc}[\omega_c(t-\tau)] \tag{23}$$

From equation (20), the approximate detected signal is therefore*

$$\begin{bmatrix} j(t) \\ j'(t) \\ j''(t) \end{bmatrix}_{DET} \simeq \frac{\omega_c}{\pi} \int_{-\infty}^{\infty} \text{Sinc}[\omega_c(t-\tau)] \begin{bmatrix} j(\tau) \\ j'(\tau) \\ j''(\tau) \end{bmatrix} d\tau \tag{24}$$

Figure 8 illustrates the Sinc transfer function, with a temporal resolution of roughly $1/2f_c$. For f_c = 100 kHz, the temporal resolution is approximately 5 μsec, which corresponds to a voltage resolution of 1/2 volt for a constant sweep speed of .1 V/μsec.

A direct connection between time and voltage response of the probe current detection network assumes the bias voltage driving the probe, $V_\phi(t)$, is a linear function of time. Nonlinearities in $V_\phi(t)$ have minimal impact on measurement of the probe characteristic, since the signal digitizer simultaneously samples both the probe bias and its corresponding probe current. The measured probe characteristic is therefore independent of the exact form of $V_\phi(t)$, within the constraints imposed by driver response and finite bandwidth effects mentioned above. Derivative measurements, however, are strongly dependent on

*The non-causal behavior of equation (24) is due to the exclusion of phase response from equation (22).

$V_\phi(t)$. Straightforward differentiation yields the relation between derivatives with respect to time and derivatives with respect to bias voltages:

$$\frac{d}{dt} = \left(\frac{dV_\phi(t)}{dt}\right) \frac{\partial}{\partial V_\phi} \tag{25}$$

$$\frac{d^2}{dt^2} = \left(\frac{d^2V_\phi(t)}{dt^2}\right) \frac{\partial}{\partial V_\phi} + \left(\frac{dV_\phi(t)}{dt}\right)^2 \frac{\partial^2}{\partial V_\phi^2} \tag{26}$$

For $V_\phi(t) \propto t$, time and voltage derivatives are directly proportional. A rough estimate of the errors incurred by a nonlinear $V_\phi(t)$ is possible by including a small second order nonlinearity in the bias voltage

$$V_\phi(t) = A_o + \alpha t + \beta t^2 \tag{27}$$

A nonlinearity of 0.5% i.e. ($Bt/\alpha \leq .005$ for all t during the pulse) will incur an error of $\leq 1\%$ in directly relating d/dt to d/dV , and an error of $\leq 2\%$ in directly relating d^2/dt^2 to d^2/dV^2.

Measured nonlinearity in the driver section depicted in Fig. 7, was less than 0.5% over the entire range of bias voltage. The resulting errors incurred in derivative measurements are therefore insignificant compared to other systematic uncertainties.

Ion Current Effects

Equations (9) and (15) relate the electron distribution function to derivatives of the electron probe current. However, since the differentiation network operates on the total probe current, it is

necessary to examine the effect of ion current on distribution function measurements.

Under the operating conditions encountered in the Berkeley source, an analytic expression for the ion current as a function of probe bias does not exist. This is primarily due to electron thermal effects which, for an ion attracting probe, allow an electric potential of approximately kT_e to exist in the quasi-neutral plasma region exterior to the plasma-probe sheath. Thus, for the case where $T_i < T_e$, ion probe current is quite insensitive to ion temperature and mainly depends on the complex relation between plasma sheath growth and probe operating parameters. To obtain the exact form of this relation requires a numerical solution of the equations which govern the behavior of ion attracting probes in a collisionless plasma.

One numerical calculation which is particularly well suited for the plasma conditions prevalent in the Berkeley source, is given by Laframboise.[2] Recall that within the Laframboise theory, ion probe current density as a function of probe bias is described by equation (1). Several approximate analytic fits to the numerical results of Laframboise have been made for a wide range of probe-plasma operating conditions.[8] For the Berkeley source, a typical analytic fit to i_+, the ion current correction factor, is given by

$$i_+(V_\phi) = \begin{cases} 0.9\,\chi^{.469} & \text{for } 0 \le \chi < 2 \quad \text{within 8\%} \\ 1.09\,\chi^{.182} & \text{for } 2 \le \chi \le 25 \quad \text{within 1\%} \end{cases} \tag{28}$$

where $\chi = \dfrac{eV_\phi}{kT_e}$. Defining R as the ratio of $j_i''(V_\phi)$ to $j_e''(V_\phi)$, and utilizing the results of equations (1), (7) and (28) yields

$$R = \frac{\left(\frac{d^2 j_1(V_\phi)}{dV_\phi^2}\right)}{\left(\frac{d^2 j_e(V_\phi)}{dV_\phi^2}\right)} = \sqrt{\frac{M_e}{M_1}}\,(kT_e)^2 e^{\chi}\left(\frac{d^2 i_+(V_\phi)}{dV_\phi^2}\right) = \begin{cases} 3.7 \cdot 10^{-3}\left(\frac{e^{\chi}}{\chi^{1.53}}\right) & \chi < 2 \\ 2.7 \cdot 10^{-3}\left(\frac{e^{\chi}}{\chi^{1.82}}\right) & \chi \geq 2 \end{cases} \qquad (29)$$

For $R < 1$, electron effects dominate, which implies from equation (29) that probe bias remain in the approximate range $.1\ kTe \leq eV \leq 10\ kTe$. In practice, uncertainties in distribution function measurement tend to limit results to well within this range.

Other Effects

A compendium of experimental complications associated with probe measurements is presented in most standard probe references.[3,4,8,9] Important effects like probe surface contamination and probe area variation can usually be minimized by careful probe/driver design. For example; as previously noted, the Probe Driver (Fig. 5) initially applies a large positive bias (~70 volts) to the probe in order to insure a clean collection surface by electron bombardment. Probe area variation is minimized by the use of a shadowed cavity probe (Fig. 9), which prevents an electrical contact from developing between the probe surface and deposited metallic materials on adjacent insulators. This technique is especially important in high current, hot cathode arcs; where tungsten plating due to ablation of the filaments is large.

Probe perturbation of the plasma is, however, unavoidable. The degree to which the perturbation effects the probe measurement is a function of probe-plasma operating conditions, and for many systems

becomes appreciable only when probe bias approaches the plasma potential, where the collected electron current is large. Regarding the probe current-voltage characteristic, this effect tends to round off the ideally sharp break occurring between the electron transition region and the electron saturation region (Fig. 2). A reasonable approximation of the plasma potential and associated electron saturation current, is customarily achieved by linearly extrapolating the two regions in the neighborhood of the break and obtaining their intersection (Fig. 2).

In distribution function measurements, the perturbation's effect appears as a depletion in the number of electrons with energy roughly less than or equal to kT_e. This effect is mitigated by the condition that for most applications, distribution function structure in this energy region can be inferred from probe characteristic measurements.

III. Measurement of the Electron Distribution Function by Harmonic Analysis

If a small A.C. potential at frequency ω_o is added to the D.C. probe bias,

$$V_\phi(t) = V_\phi^o + v \cos(\omega_o t) \tag{30}$$

where

$V_\phi^o \equiv$ D.C. probe bias

$v \equiv$ A.C. probe bias amplitude

then the corresponding probe current density as a function of probe bias can be expressed in terms of its Taylor Series expansion about V_ϕ^o;

$$j(V_\phi) = j(V_\phi^o) + v\cos(\omega_o t)\left.\frac{dj(V_\phi)}{dV_\phi}\right|_{V_\phi = V_\phi^o} + \frac{v^2}{2}\cos^2(\omega_o t)\left.\frac{d^2 j(V_\phi)}{dV_\phi^2}\right|_{V_\phi = V_\phi^o}$$

$$+ \frac{v^3}{6}\cos^3(\omega_o t)\left.\frac{d^3 j(V_\phi)}{dV_\phi^3}\right|_{V_\phi = V_\phi^o} + \cdots \qquad (31)$$

Noting the trigonometric identities:

$$\cos^2(\omega_o t) = 1/2\left\{\cos(2\omega_o t) + 1\right\}$$

$$\cos^3(\omega_o t) = 1/4\left\{\cos(3\omega_o t) + 3\cos(\omega_o t)\right\}$$

$$\cos^4(\omega_o t) = 1/8\left\{\cos(4\omega_o t) + 4\cos(2\omega_o t) + 3\right\}$$

and substituting into equation (31) yields,

$$j^{2\omega}(V_\phi^o) = \frac{v^2}{4}\left.\frac{d^2 j(V_\phi)}{dV_\phi^2}\right|_{V_\phi = V_\phi^o} + \frac{v^4}{48}\left.\frac{d^4 j(V_\phi)}{dV_\phi^4}\right|_{V_\phi = V_\phi^o} + \cdots \qquad (32)$$

where $j^{2\omega}(V_\phi^o)$ is the spectral component of the probe current density at frequency $2\omega_o$ and D.C. bias V_ϕ^o (i.e. $j(V_\phi^o, 2\omega_o) = j^{2\omega}(V_\phi^o)\cos(2\omega_o t)$). Neglecting higher order terms in equation (32), and substituting into equation (9),

$$j_e^{2\omega}(V_\phi^o) \propto \frac{\pi v^2 e^3}{2m_e^2}\left. f_e(\varepsilon)\right|_{eV_\phi = \varepsilon} \qquad (33)$$

which relates the electron energy distribution function to the second harmonic component of the electron probe current density.

Figure 10 schematically illustrates the harmonic detection network. The network consists of four main sections; the probe driver (previously described), the driving signal network which supplies A.C. probe bias, the reference frequency generator or frequency doubler, and a phase

sensitive lock-in detector. In the driving signal network (Fig. 11A), the output of a sine wave generator is filtered by a tuned amplifier (Q ~ 40) composed of μA 741 op amps, which limits the total harmonic distortion of the driving signal to less than .04% at output. Isolation amps, composed of μA 741 voltage followers, provide buffering to avoid resonant interaction among stages.

Outputs of the driving signal network are applied to the sum point of the probe driver op-amp, where a variable D.C. bias is added; and to the frequency doubling network (Fig. 11B), which provides a reference signal at the second harmonic. The probe network supplies a constant amplitude A.C. bias over the entire range of D.C. bias values. Nonlinearities in the probe current-voltage characteristic generate harmonic distortion of the fundamental driving frequency, which is differentially detected by a lock-in amplifier. The filtered harmonic content of the probe current is mixed with the reference frequency, time integrated to minimize noise effects, and recorded by a storage scope; the recorded signal being directly proportional to the second harmonic content of the probe current.

IV. Accuracy Analysis of the Harmonic Technique

Several of the effects previously mentioned in the accuracy analysis of the pulsed probe detection network apply to the harmonic technique as well. In particular, analysis of probe/plasma response (for $\omega_o \ll \omega_{pi}$), ion current effects, shot to shot reproducibility, probe perturbation of the plasma etc. are practically identical for the two techniques. In addition, accuracy of the harmonic technique

depends on non-ideal circuit effects in the harmonic detection network, and the effect of higher order derivatives on the probe current second harmonic content (equation 32).

Since the harmonic technique employs the non-linear property of the probe characteristic, nonlinearities in the detection network (Fig. 10) will induce systematic errors (circuit related harmonic distortion) in distribution function measurements. Also, the non-ideal behavior (due to finite bandwidth effects) of tuned amplifiers in the driving signal network and lock-in amplifier, can cause systematic error due to non zero mixing of fundamental frequency components. If necessary, this effect can be minimized by designing the apparatus to detect intermodulation rather than harmonic distortion.[10]

In general, the simple relation between the electron energy distribution function and the probe current second harmonic content (Eq. 33), may not be completely valid if higher order derivatives in Eq. 32 are significant. A generalized form of Eq. 33 is obtainable by recalling the previously derived relation describing electron probe current as a function of bias:

$$j_e(V_\phi) = \frac{2\pi e}{m_e^2} \int_{eV_\phi}^{\infty} \varepsilon f_e(\varepsilon) \left(1 - \frac{eV_\phi}{\varepsilon}\right) d\varepsilon \tag{5}$$

where for the apparatus described in Fig. 10,

$$V_\phi = V_\phi^o + v \cos(\omega_o t) \tag{30}$$

Letting $\cos(\omega_o t) = X$, $j_e(V_\phi)$ can be expanded in a Chebyshev power series about V_ϕ^o:

$$j_e(V_\phi) = 1/2\ j_e^o(V_\phi^o) + \sum_{K=1}^{\infty} j_e^{K\omega}(V_\phi^o)\ T_K(X) \tag{34}$$

where

$$j_e^{K\omega}(V_\phi^o) = \frac{2}{\pi} \int_{-1}^{1} j_e(V_\phi) \frac{T_K(X)}{\sqrt{1 - X^2}} dX \tag{35}$$

is the spectral component of the electron probe current density at frequency $K\omega_o$ and D.C. bias V_ϕ^o, and $T_K(X)$ is a Chebyshev Polynomial of degree K. Thus, the second harmonic component of $j_e(V_\phi)$ is

$$j_e^{2\omega}(V_\phi^o) = \frac{2}{\pi} \int_{-1}^{1} j_e(V_\phi) \frac{T_2(X)}{\sqrt{1 - X^2}} dX \tag{36}$$

Substituting for $j_e(V_\phi^o)$ from Eq. 5, and V_ϕ from Eq. 30,

$$j_e^{2\omega}(V_\phi^o) = \frac{4e^2 v}{m_e^2} \int_{-1}^{1} dX \frac{T_2(X)}{\sqrt{1 - X^2}} \int_{e(V_\phi^o + vX)}^{\infty} (\alpha(\varepsilon) - X) f_e(\varepsilon)\, d\varepsilon \tag{37}$$

where

$$\alpha(\varepsilon) = \left(\frac{\varepsilon - eV_\phi^o}{ev} \right) \tag{38}$$

Interchanging the order of integration yields,

$$j_e^{2\omega}(V_\phi^o) = \frac{4e^2 v}{m_e^2}\left[\int_{e(V_\phi^o - v)\geq 0}^{e(V_\phi^o+v)} f_e(\varepsilon)\, d\varepsilon \int_{-1}^{\alpha(\varepsilon)} (\alpha(\varepsilon) - \chi)\frac{T_2(\chi)}{\sqrt{1-\chi^2}}\, d\chi + \int_{e(V_\phi^o+v)}^{\infty} f_e(\varepsilon) d\varepsilon \int_{-1}^{1} (\alpha(\varepsilon) - \chi)\frac{T_2(\chi)}{\sqrt{1-\chi^2}}\, d\chi\right] \tag{39}$$

Integrating over X, and defining the function

$$\kappa(V_\phi^o, \varepsilon) = ev\left(1 - \left(\frac{\varepsilon - eV_\phi^o}{ev}\right)^2\right)^{3/2} \qquad (-ev \leq \varepsilon - eV_\phi^o \leq ev)$$
$$= 0 \qquad (|\varepsilon - eV_\phi^o| \geq ev) \tag{40}$$

yields,

$$j_e^{2\omega}(V_\phi^o) = \frac{4e}{3m_e^2}\int_0^\infty \kappa(V_\phi^o, \varepsilon) f_e(\varepsilon)\, d\varepsilon \tag{41}$$

Equation 41 is the generalized form of Eq. 33, including higher order effects. The function $\kappa(V_\phi^o,\varepsilon)$ (Fig. 12) acts like a network transfer or instrument function analogous to Eq. 24.* Qualitatively, $\kappa(V_\phi^o,\varepsilon)$ tends to smear out distribution function structure on a scale smaller

*Equation 41, like equation 24 can be solved to yield an exact form of $f_e(\varepsilon)$ via the technique of numerical deconvolution.[11,12] However experimentally, judicious circuit design (in the case of equation 24) and minimal A.C. bias (in the case of equation 41) will yield instrument functions whose half widths ($\Gamma_{1/2}$) are considerably less than the energy spread characterizing distribution function structure (i.e. for a Maxwellian, $\Gamma_{1/2} \ll KT_e$). Thus, the errors incurred by not deconvoluting equations 24 or 41, are minimal with respect to other experimental considerations.

than v, the A.C. bias amplitude. Typical experimental values of v, chosen to maximize resolution and signal to noise effects, range from .3v to .8v.

EXPERIMENTAL RESULTS

I. A Brief Overview

Figure 13 shows a typical set of experimental data obtained by the pulsed probe system. The data consists of a cylindrical probe characteristic and its first and second derivatives. Note that the position of the cursor, indicated by the intersection of the horizontal and vertical fiducial lines, is an artifact of the digital recorder and does not mark the position of a coordinate origin. The first of the digitized coordinates appearing in each of the photographs indicates the plasma potential. Determination of the plasma potential from distribution function measurements agrees, within experimental uncertainty, with the value obtained from the probe characteristic. The data set was taken with a radial probe at source center, an arc power of 16.3 kw, and deuterium input flow of 6.5 T-ℓ/sec.

Figure 14A is a logarithmic plot of the electron probability distribution function $f_e(\varepsilon)$. Figure 14B plots the total electron energy distribution function $F_e(\varepsilon)$, including phase space weighting (i.e. $F_e(\varepsilon) \propto f_e(\varepsilon)\sqrt{\varepsilon}$, where $F_e(\varepsilon)d\varepsilon$ gives the relative number of electrons with energy between ε and $\varepsilon + d\varepsilon$). The distribution function is typical of the Berkeley source and consists of cool, thermal electrons which are electrostatically confined by the source wall floating potential, plus a component of high energy, non thermal primaries and degraded primaries. The bulk thermal electrons comprise roughly 90 to 98 percent of the total electron density depending on operating conditions. Both plots were obtained by averaging over multiple data sets similar

to Fig. 13C. Error bars indicate random uncertainties associated with the experimental measurement and averaging processes. Systematic errors are not explicitly indicated, but their effects are visible. The solid line in Figs. 14A and 14B, plots a Maxwellian with $kT_e = 3.8$ eV; the bulk electron temperature measured by probe characteristic (Fig. 14C). For energies less than ~2 eV, measured values fall systematically below the Maxwellian curve due to probe perturbation effects. Finite bandwidth effects (Eq. 24), also tend to smear out distribution function structure on a scale less than ~1/2 eV.

Figures 14C and 14D are the corresponding computer generated logarithmic plots of the electron probe current, and its first derivative as a function of probe bias, respectively. Both plots clearly indicate an enhanced population of high energy electrons, in agreement with distribution function measurements. The indicated error bars include effects due to uncertainties in probe area, detector resistance, ion current, detection amplifier drifts, and quantisation error of the signal digitizer. Finite bandwith effects, not explicitly shown, tend to smear out structure in the recorded data on a scale less than .1v (.5v) for the probe characteristic (first derivative) respectively. The probe characteristic is analyzed by an on line computer routine which outputs the plasma potential, bulk electron temperature, electron and ion density, and their respective uncertainties. The uncertainties in these quantities include systematic effects due to probe perturbation and finite bandwidth. Measurement of the bulk electron temperature by the probe characteristic and its 1st derivative, are consistent with distribution function measurements as shown in Fig. 14.

As previously cited, measurements of the electron distribution function by harmonic analysis were performed as an auxiliary check on results obtained by the pulse probe technique. One example of a comparison between distribution functions measured by the two techniques, under conditions previously stated (Fig. 14), is illustrated in Fig. 15. The indicated error in harmonic measurement, include non-ideal circuit effects and resolution limitations (Eq. 41) previously described. Excellent agreement between the two independent measurements serves to confirm the reliability of both techniques.

II. The Electron Distribution Function

Preliminary analysis of the electron distribution function in low pressure, hot cathode discharges was performed by Langmuir in 1925.[13] Employing the technique of electrostatic probes,[14] current-voltage characteristics were obtained for a variety of operating conditions in low current (~10mA), D.C. mercury vapor discharges. These probe characteristics, in many ways similar to those obtained in the Berkeley source (Figure 14C), were interpreted by Langmuir as being derivable from an electron distribution function composed of three main constituents:

1. Primary electrons: thermionically emitted electrons energized by their passage through the cathode-plasma sheath.
2. Secondary electrons: an isotropic, thermal constitutent with a temperature considerably less than, but dependent on the primary electron energy. In Figure 14C, the electron probe current due to secondary electrons would roughly correspond

to probe bias between 0 and 23 volts. Note that the secondary electrons appear thermal, due to the exponential dependence of probe current on probe bias in this range (Equation 7).

3. Ultimate electrons: a cool isotropic, thermal constituent constituting the bulk of the electron population with a temperature less than the secondaries, but fairly independent of primary electron energy. In Figure 14C, the ultimate's contribution corresponds to probe bias between 23 volts and the plasma potential. Again, note that the ultimate electrons appear thermal.

The secondary and ultimate electrons compose what is often called a two temperature or Bimaxwellian distribution function. However, the physical origin of this distribution function is difficult to resolve. For high energy electrons comprising a majority of the secondary population, the collisional mean free path is many times greater than the plasma's spatial dimension and hence, collisional relaxation is inadequate to account for thermalization. Several explanations of this apparent conundrum, ofttimes called "The Langmuir Paradox," have been proposed involving collective effects such as plasma-sheath oscillations.[15] In recent years, subsequent experimental investigations of low current discharges have provided evidence that questions pertaining to the resolutions of Langmuir's Paradox are possibly moot. Work by Rayment and Twiddy,[16] involving direct distribution function measurement via the harmonic double differentiation technique in mercury vapor discharges, have shown that the electron distribution function is non thermal, despite the thermal nature indicated by probe characteristic measurements.

With regard to the Berkeley source, distribution function measurements performed under relatively high discharge current conditions, confirms the non thermal nature of the distribution function tail.* As previously noted, Figures 14A and 14B plot the electron probability distribution function ($f_e(\varepsilon)$) and the total electron energy distribution function ($F_e(\varepsilon)$) respectively, under typical source operating conditions. The distribution function, in contrast to Langmuir's interpretation, consists of two main constituents:

1. Thermal bulk electrons which constitute the majority of the total electron population (roughly 96% for the function shown in Figure 14B).

*On the basis of careful statistical analysis involving probe characteristic measurements obtained over a wide range of source operating conditions, the Bimaxwellian model of the electron distributed function also fails to fit all experimental data. Confidence levels of the χ^2 fit parameter:

$$\chi^2 = \sum_N \frac{\left[i_{exp}(\varepsilon_N) - i_{the}(\varepsilon_N)\right]^2}{\sigma_N^2}$$

where:

$N \equiv$ The numbers of discrete data samples

$\sigma_N^2 \equiv$ Effective experimental variance (error)

$i_{exp}(\varepsilon_N) \equiv$ Experimentally measured probe current at energy ε_N.

$i_{the}(\varepsilon_N) \equiv$ Theoretically predicted probe current at energy ε_N based on the Bimaxwellian model.

were insufficient to accept the Bimaxwellian model for all data sets.

2. A non thermal high energy tail, which comprises the monotonically decreasing high energy component of the distribution function (Figure 16A).*

The break between the bulk electron component and non thermal tail, occurs at an energy roughly corresponding to the potential difference between the plasma potential and the source wall floating potential. Measurements made with cylindrical probes oriented in the axial and radial directions, and with spherical probes confirm the near isotropy of the distribution function. This isotropy, primarily due to the symmetry of the source chamber, is in contrast with the anisotropic distribution functions measured by Twiddy et al in positive column discharges.

Qualitatively, distribution function structure is best understood by considering the source chamber as an electrostatic potential well. Excluding the anode, the chamber consists of several electrically isolated sections of conducting wall; each section floating negative with respect to the plasma potential such that the net random current due to electron and ion bombardment is nulled.** Source walls therefore form a potential

---

*Recent theoretical work by Cary,[17] proposes an algorithm for computing the non thermal tail via a purely collisional model. Agreement between expeimentally measured and theoretically generated probe characteristics, over a wide range of source operating conditions, is within limits set by experimental uncertainties.

**Differences in the floating potential of adjacent wall sections are primarily due to the spatial dependence of electron and ion flux within the plasma. However, for purposes of discussion, all walls can be assumed to float at a uniform potential.

well for electrons; the containment condition being that the projected energy of an electron normal to a wall surface ($\varepsilon_\perp$), is less than the potential difference between the plasma potential and the wall floating potential ($\Delta\varepsilon_{WELL}$). This containment condition can be employed to conceptually dichotomize the distribution function into the two constituents described above.

1. Electrons whose total energy is less than $\Delta\varepsilon_{WELL}$, and which remain trapped until encountering the anode. Electrons in this group can be shown to have sufficient time to thermalize before escaping,[17] and hence constitute the bulk thermal electrons.

2. Electrons whose total energy is greater than $\Delta\varepsilon_{WELL}$ (the high energy tail). Within this group, electrons where $\varepsilon_\perp < \Delta\varepsilon_{WELL}$ will remain trapped until collection by the anode, an inelastic encounter with a background neutral, or scattering into the "loss cone" defined by the condition $\varepsilon_\perp > \Delta\varepsilon_{WELL}$. The containment period, which for typical source operating conditions is $\sim$.03 μsec, is insufficient to allow thermalization,[17] but evidently sufficient to insure no overall depletion of the tail.

Spatially, $F_e(r,\varepsilon)$ remains fairly constant over the majority of source volume. Radial and axial scans of bulk electron temperature (Figures 20A, 20B, and 21A) show a fair degree of spatial uniformity. Radially, $F_e(r,\varepsilon)$ exhibits a gradual enhancement of the high energy tail with increasing radial position. This effect can be partially attributed to the high energy containment condition ($\varepsilon_\perp < \Delta\varepsilon_{WELL}$)

which, for the cylindrical geometry of the source chamber, favors energetic electrons with small radial velocity components that can elastically scatter off the plasma-wall sheath. Since the high energy tail is responsible for plasma ionization, its radial enhancement performs the beneficial function of flattening the plasma's potential and density profile; a necessary condition for useful ion extraction (see Section III). Figure 16B illustrates the distribution function tail near the filaments at a radial position 6 cm off axis. The tail comprises ~10% of the total electron population as opposed to ~4% for Figure 16A obtained under the same operating conditions on axis. In terms of electron population capable of ionization, this relates to an off axis density of $\sim 1.6 \cdot 10^{11}/cm^3$ as compared to $1.2 \cdot 10^{11}/cm^3$ on axis; even though the total electron density maximizes at source center (see Figure 20).

The High Energy Tail Beyond Cathode Fall

The existence of electrons with energy values exceeding the cathode fall in electrical discharges have been documented since the early days of vacuum tubes.[18] An extensive study of this effect in low current, hot cathode discharges was initially performed by Langmuir.[13] Using probe characteristic measurements, substantial electron currents were measured for probe bias values up to -20 volts with respect to cathode. Langmuir attributed this effect to primary electron scattering, and proposed an algorithm for determining the temperature by hypothesizing an isotropic Maxwellian, displaced in energy by cathode fall acceleration:

$$f_p(\varepsilon) = n_e \left(\frac{m_e}{2\ kT_e}\right)^{3/2} e^{-(\sqrt{\varepsilon} - \sqrt{eV_p})^2/kT_p} \qquad (42)$$

where $V_p \equiv$ Plasma Potential w.r.t. cathode

$T_p \equiv$ Primary Temperature

as the primary electron distribution function. For a 5mA low pressure mercury vapor discharge, with a cathode fall of 50 volts, a primary temperature of .12 eV was sufficient to account for the experimental measurements.

Similar measurements performed on the Berkeley source, involving high resolution probe characteristics, generally concur with Langmuir's experimental results. Figure 17 is a computer plot of a probe characteristic obtained under conditions similar to those of Figure 14. Measurable electron current extends to probe bias values 20 volts negative of (-) filament. (Zero bias marks the negative leg of the filaments.) For purpose of comparison, a displaced Maxwellian description of the primary distribution function (equation 42), when incorporated into the equation describing general probe current as a function of probe bias (equation 5), yields:

$$j_p(V_\phi) = en_e \left(\frac{1}{2\pi m_e}(kT_p)^3\right)^{1/2} \int_{eV_\phi}^{\infty} \varepsilon\left(1 - \frac{eV_\phi}{\varepsilon}\right) e^{-(\sqrt{\varepsilon} - \sqrt{eV_p})^2/kT_p} d\varepsilon \qquad (43)$$

The spread in primary energy due to filament emission can be numerically simulated by a sum over energy intervals, each interval consisting of a beamlet described by equation (43). Thus,

$$j_p(V_\phi) \propto \sum_{N=1}^{N_{MAX}} \int_{eV_\phi}^{\infty} \varepsilon\left(1 - \frac{eV_\phi}{\varepsilon}\right) e^{-(\sqrt{\varepsilon} - \sqrt{\varepsilon_N})^2/kT_p} \, d\varepsilon \qquad (44)$$

where $\varepsilon_N \equiv$ the cathode fall potential for beamlet N. Figure 17 illustrates a fit of equation (44) to probe data for fit parameters kT_p and $\Delta\varepsilon_N$, where $\Delta\varepsilon_N \equiv \varepsilon_{NMAX} - \varepsilon_1$, represents the spread in primary energy due to filament emission. The results indicate an optimum fit for $\Delta\varepsilon_N = 9$ eV and $kT_p = 1.8$ eV which, allowing for the inherent limitation in the analysis, indicates a primary energy spread. Direct temperature determination from the probe characteristic yields $kT_p \sim 4.8$ eV.

A more precise determination of the high energy tail at energy values exceeding cathode fall entails direct distribution function measurement. Measurements performed in low current discharges reveal a monotonically decreasing function over a range 15 to 20 eV greater than cathode fall. The dominant mechanism for this primary scattering is due to a resonant interaction between the primary and bulk plasma electrons. The distance traveled by primaries before being strongly scattered is roughly 1/10 the collisional mean free path for electron-electron scattering, and corresponds to a plasma interaction time of approximately three plasma periods; indicating a strong beam-plasma effect.[16]

Analogous measurements on the Berkeley source are, in general, difficult due to the low signal to noise ratios encountered with small cylindrical or spherical probes. However, by using a section of axially symmetric floating wall as an extended wall probe, measurements are

possible under low density discharge conditions (an instrumental limitation). Figure 18 illustrates an axially projected distribution function obtained for a background plasma density of $1 \cdot 3 \cdot 10^{12}/cm^3$ (Discharge arc power = 10.3 kW). The results parallel those of Rayment and Twiddy, and consist of a monotonically decreasing function out to 20 eV above cathode fall.

Summary

The electron distribution function measured in the Berkeley source, consists of a component of thermal electrons comprising the bulk electron population which exist for $\varepsilon \leq \Delta\varepsilon_{WELL}$; and a non thermal high energy tail which is a monotonically decreasing function of energy and contains a small, but experimentally significant, electron population at energy values 15 to 20 eV above cathode fall.

When computing bulk plasma properties such as electron Debye length, which sets the spatial scale determining sheath structure, the distribution function may be considered thermal at the bulk electron temperature. However, when computing dissociation and ionization rates, the high energy tail has profound influence. For example, the population of ionizing electrons in deuterium is typically 100% larger than expected from a Maxwellian at the bulk electron temperature. The enhancement of ionization rates is even greater due to cross section weighting. Overall ion production can be considered roughly uniform throughout the source volume with an added correction due to radial enhancement.

A collisional model algorithm for computing distribution function structure at energy values less than the cathode fall, has been proposed.

Model predictions of electron probe current characteristics agree with experimental measurements within allowed variance. Models describing distribution function structure for energy values greater than cathode fall, can possibly be inferred from similar measurements in low current discharges where beam-plasma interactions dominate. However at present, no direct experimental confirmation of this mechanism in the Berkeley source exists.

III. The Spatial Dependence of Source Plasma Parameters

The first comprehensive steady state theory of a low pressure, magnetic field free discharge was formulated by Tonks and Langmuir in 1929.[19] The theory involved solution of Poisson's equation under conditions where:

1. electrons are assumed to have a Maxwellian distribution function; their local density satisfying the Boltzman relation $n_e(X) \propto \exp(e\phi(X)/kT_e)$ where $\phi(X)$ is the local plasma potential.
2. ions are assumed created at rest throughout the plasma volume according to a specified generation function, and subsequently free fall without collision in the local ambipolar electric field to the walls, where recombination with electrons occur. For the case of planar, cylindrical or spherically symmetric discharges ($\beta = 0, 1, 2$ respectively), the ion continuity equation under the free fall and steady state assumptions, yields the local ion density function:

$$n_i(X) = \left(\frac{M_i}{2e}\right)^{1/2} \frac{1}{X^\beta} \int_o^X \frac{G(Y)\, Y^\beta dY}{[\phi(Y) - \phi(X)]^{1/2}} \qquad (45)$$

where $G(X) \equiv$ Ion generation rate per unit volume

$\phi(X) \equiv$ Local plasma potential (a monotonically decreasing function of X, with $\phi(0) = 0$)

$X \equiv$ Variable characterizing the spatial position in the discharge measured with respect to the center of symmetry (i.e., X = Z; r for planar; cylindrical or spherical discharges, respectively).

Thus Poisson's equation becomes:

$$\nabla^2 \phi(X) = -4\pi e(n_i(X) - n_e(X))$$

$$= -4\pi e \left[\left(\frac{M_i}{2e}\right)^{1/2} \frac{1}{X^\beta} \int_o^X \frac{G(Y) Y^\beta dY}{[\phi(Y) - \phi(X)]^{1/2}} - n_{eo}\, e^{(e\phi(X)/kT_e)} \right] \qquad (46)$$

Langmuir termed this result "The complete plasma-sheath equation" and proposed solutions for two simplified but physically interesting cases:

1. The plasma approximation, where quasi-neutrality requires $\nabla^2\phi(X) = 0$.
2. The thin sheath approximation where volume ion production in the sheath region can be ignored.

The proposed solutions were in power series form, and were asymptotically correct in the limit of small Debye length.

Exact solutions of equation 46 for planar discharges; and asymptotic, thin sheath solutions of equation 46 for cylindrically and spherically symmetric discharges, were formulated by Self assuming plasma ion

production spatially uniform, proportional to the electron density, and proportional to the square of the electron density.[20,21] Since many relevant discharge parameters are calculable once the potential distribution is known, these solutions provide valuable input for predicting ion source performance. However, for most experimental discharge chambers, a two dimensional generalization of the Self solutions are necessary in order to obtain a complete and accurate spatial mapping of the plasma potential.

The integro-differential form of equation 46 makes dimensional generalization difficult. An alternative approach to steady-state low pressure discharge theory, proposed by Kino and Shaw,[22] retains the Maxwellian assumption for electrons, but treats ion motion via transport equations obtained from moments of the Boltzman equation. Hence, whereas the Tonks-Langmuir or Self method deals with an exact description of ion motion in terms of the ion distribution function and related local ion density (equation 45), the moment method employs a macroscopic fluid description of ion motion in terms of the fluid velocity $\vec{v}_i$, the pressure tensor $\overleftrightarrow{P}_i = M_i n_i \langle \vec{w}_i \vec{w}_i \rangle$ where $\vec{w}_i$ is the random ion velocity, and the heat flow tensor $\overleftrightarrow{Q}_i = M_i n_i \langle \vec{w}_i \vec{w}_i \vec{w}_i \rangle$. Employing only the first two moment equations (continuity and momentum transfer) and closing the set with the assumption $\overleftrightarrow{P}_i = 0$ (which neglects kinetic pressure effects), results in rough agreement with Self's calculations. By retaining the third moment equation (heat transfer) and closing the set with the adiabatic assumption $\nabla \cdot Q_i = 0$, very close agreement is obtained.

The advantage of the moment equation method, is that it leads to differential equations which are easier to generalize and compute than the exact plasma sheath equation (46). For planar or cylindrically symmetric discharges, the equations spatially decouple into their respective orthogonal dimensions.* Hence for the 10 amp source, the spatial potential profile is approximately given by:

$$\phi(r,Z) = \phi(r) + \phi(Z) \tag{47}$$

where $\phi(r)$, $\phi(Z)$ are the radial, axial potential profiles respectively. The general forms of $\phi(r)$ and $\phi(Z)$ are similar to their analogous one dimensional Self solutions.** However exact axial and radial potential profiles are dependent on R/L_z, the source radius to depth ratio, and therefore must be obtained from the full two dimensional treatment. Unfortunately, published solutions are limited and hence, in general, exact solutions require extensive numerical computations.

---

*This statement is exactly correct only for the case where ion production is proportional to the electron density ($\gamma = 1$).[23] For the general case of ion production, spatial decoupling requires ion motion satisfy the condition $(\vec{v}_i \times \nabla\phi) \sim 0$, which physically states that ions follow electric field lines. This assumption is approximately satisfied over the bulk of the discharge chamber, where field line curvature is minimal, if $(T_i/T_e) \ll 1$.

**For example, in cylindrically symmetric discharges where plasma ion production is proportional to the local electron density, potential profile in the vicinity of the discharge center will fit one dimensional planar theory axially to within 10% for $R/L_Z \gtrsim 12$, and fit one dimensional cylindrical theory radially to within 10% for $R/L_Z \lesssim 0.9$.[23]

Experimental Measurements

Experimental determination of the spatial dependence of source plasma parameters involved obtaining axial and radial probe characteristics for several sets of source operating conditions. The measurements include both bulk electron temperature, plasma potential, plasma density, and saturated ion current density as a function of axial and radial position. A schematic illustrating the axial and radial probe positions with respect to the source chamber is shown in Figure 19. The axial probe sits 1 4 cm off axis, but for all practical purposes can be expected to measure on axis parameter values due to their weak radial dependence in this region. The radial probes sit in a plane 2.2 cm off the backwall, which essentially bisects the cylindrical floating wall or barrel section (see Figure 1A).

The radial and axial probe scans are illustrated in Figures 20 and 21. All data points represent composite values obtained by averaging over multiple data sets in order to reduce experimental uncertainties.*

*A warm up period of between 60 and 90 shots, resulting in a total operating time of 6 to 9 seconds, was required in order to insure good shot to shot reproducibility in plasma potential measurements. Under cold conditions, the plasma potential would initially sit 3 to 4 volts below anode potential, gradually increasing from shot to shot until reaching a steady state value 1 to 2 volts below anode. This effect tends to imply an initial small contamination of easily ionizable material in the background gas, possibly due to wall outgassing, which is subsequently halted by fresh tungsten deposition on chamber walls from filament ablation. Measurements of bulk electron temperature, plasma density, and saturated ion current density were essentially unaffected by the potential drift.

Plasma density values are comprised of independently obtained electron and ion density measurements. Saturated ion current densities are defined in terms of the normalized value:

$$j_i)_{SAT} = \frac{1}{4} N_i e \sqrt{\frac{8kT_e}{\pi M_i}} \tag{48}$$

and hence will roughly be a factor of 2 smaller than values obtained from actual probe measurements, due to omission of the probe sheath correction factor (see equation 1). The normalized values are, however, close to the extractable ion current densities predicted by ion free fall models.

Figures 20A and 20B illustrate radial profile data for arc power values of 16.3 kW and 21.6 kW respectively. The ion free fall profile for plasma potential represents a radial solution to equation 46 for the case of spatially uniform ion production. As previously mentioned, exact solutions of the potential require a full two dimensional treatment, although for the 10 amp source where $R/L_Z \sim 1.1$, the one dimensional radial solution remains a fairly good approximation across the bulk of the discharge chamber.[23] Note that the measured profile appears slightly flatter than the free fall curve. This effect is consistant with:

1. The radial enhancement of ionizing electrons as mentioned in Section II

2. The axial position of the radial probe acquisition plane. Equipotential calculations indicate a flattening of the radial profile as a function of axial distance from source center.[23]

Ion free fall curves for plasma density and saturated ion current density are related to the plasma potential profile via the Boltzman factor at the bulk electron temperature.

Figure 21A illustrates axial profile data corresponding to the radial data of Figure 20A. The free fall curve maps a planar solution of equation 46 for spatially uniform ion production, and is intended only to convey the general form of the profile. Its asymmetry with respect to source center is presumably due to the enhancement of ionizing electrons near the front floating grid. This effect is illustrated by the electron probe current characteristics obtained near source front (floating grid) and rear, and plotted in Figures 21B and 21C respectively.

Collisional Effects

The analysis of collisional effects on ion free fall theory is probably best approached via the moment equations previously described. In the Berkeley source, where "non ideal" factors such as multiple neutral/ion species (D^o,D_2^o,D^+,D_2^+,D_3^+) and finite ion temperature* complicates

---

*Ion temperature is presumed to fall between lower limit estimates inferred from background gas temperature measurements (~.3eV for D^o, .1eV for D_2^o),[24] and upper limit estimates set by extracted beam divergence[2] (~1eV).[25]

analysis, exact solutions generally require numerical computation. However, existing two dimensional collisional solutions by Shaw,[23] for the case where plasma ion production is proportional to the local electron density, are sufficient to draw the following qualitative conclusions.

1. Collisional effects are a monotonically increasing function of $(\nu^P_{eff}/\nu^I_{eff})$, where ν^P_{eff} is the effective momentum transfer collision frequency for ions, and ν^I_{eff} is the effective ionization frequency.
2. The effect of collisions on observable plasma characteristics:
   a) reduces ion flux to the discharge chamber walls with respect to free fall theory predictions. Physically, this effect manifests the reduced ion density necessary to maintain the discharge due to an increased ion containment time.
   b) steepens the plasma's spatial profile, and approaches mobility dominated diffusion for $(\nu^P_{eff}/\nu^I_{eff}) >> 1$.

With respect to the Berkeley source, the dominant interactions among the plasma's ion constituents consist of the charge exchange collisions:[26]

$$D^+ + D^o \rightarrow D + D^+ \qquad \sigma(kT_+ \lesssim 1 \text{ eV}) \sim 6 \cdot 10^{-15} \text{ cm}^2 \qquad (49)$$

$$D_2^+ + D_2^o \rightarrow D_2 + D_2^+ \qquad \sigma(kT_+ \lesssim 1 \text{ eV}) \lesssim 1 \cdot 10^{-15} \text{ cm}^2 \qquad (50)$$

Recent calculations by Chan,[27] have indicated that typical operating conditions yield constituent ratios of $(n_D/n_{D_2}) \sim 2$ and $(n_{D^+}/n_{D_2^+}) \sim 2.7$. Under the operating conditions illustrated in Figures 20A and 21A, the

background neutral density is roughly* $n_{D_2}o \sim 3 \cdot 10^{13}$ /cm^3 and $n_D o \sim 7 \cdot 10^{13}$ /cm^3; yielding mean free paths of

$$\lambda_{D^+} = 1/(n_D \sigma_{DD^+}) \sim 2.4 \text{ cm} \tag{51}$$

$$\lambda_{D_2^+} = 1/(n_{D_2} \sigma_{D_2 D_2^+}) \sim 30 \text{ cm} \tag{52}$$

A rough estimate of "collisionality" in the Berkeley source is now possible by noting:

1. The effective ionization frequency, assuming steady state, is equivalent to the mean ion lifetime. Hence, under quasi free fall conditions,

$$\nu^I_{eff} = 1/\tau_i \sim \langle v_i \rangle / L \tag{53}$$

where τ_i is the mean ion lifetime, $\langle v_i \rangle$ is the mean ion velocity, and L represents the source spatial scale length.

2. The effective momentum transfer collision frequency is dominated by atomic charge exchange, and is approximately

$$\nu^P_{eff} \sim \langle v_i \rangle / \lambda_{D^+} \tag{54}$$

Therefore,

$$(\nu^P_{eff} / \nu^I_{eff}) \sim L/\lambda_{D^+} \lesssim 2^{**} \tag{55}$$

For this collision ratio, two dimensional collisional solutions[23] yield experimentally insignificant corrections to ion free fall

---

* An estimate of the relation between input gas flow and background neutral density, based on steady state balance between input and output flow rates, concludes that an input flow of 1 T-ℓ/sec corresponds to a neutral density of $2 \pm 1 \cdot 10^{13}$ /cm^3. This estimate concurs with the calculated estimates of Chan for typical operating conditions.[27]

** This ratio probably indicates a worst case estimate since D_2^+ ions are not considered.

model predictions. This result concurs with experimental measurements of axial and radial plasma profiles (Figures 20A, 20B, and 21A), and extracted ion current densities which agree with free fall predictions to within experimental accuracies.

Conclusions/Summary

Although existing experimental and theoretical work does not provide a complete description of the spatial dependence of plasma parameters in the 10 amp source, it remains sufficient to draw the following conclusions.

1. Overall source performance follows steady state low pressure discharge theory. In particular:
   a) Plasma potential measurements exhibit the general ambipolar profile predicted by solutions of the collisionless plasma sheath equation (46) for spatially uniform ion production.
   b) Local plasma density is related to local potential via the Boltzmar factor at the bulk electron temperature.
2. For the "pillbox" configuration of the 10 amp source, where $R/L_z \sim 1.1$, an accurate spatial mapping of the potential requires a two dimensional generalization of equation 46. This is most readily accomplished by the moment equation method proposed by Kino and Shaw. Relevant consequences of the two dimensional generalization are:
   a) The radial potential profile is a function of axial position; a profile flattening occuring as the axial distance from source center is increased.

b) Regarding ion extraction; the radial electric field imparts transverse energy to axially moving ions. Hence, ion current density at the extractor grid is a vector quantity whose angle with respect to z (normal to the extractor grid surface), is an increasing function of radius. For an extraction area of 49 cm^2, typical operating conditions yield a maximum transverse ion energy of roughly 1 eV.

3. Determination of the effects of multiple ion species,* ion temperature, and ion collisions on observable plasma parameters, requires numerical solutions of the appropriate moment equations. However, measurements indicate that these effects are minimal, and conclude that the source follows collisionless discharge theory to within experimental uncertainties.

* A multiple species generalization of the one dimensional moment theory of Kino and Shaw has been proposed by Bromberg.[28]

IV. Plasma Parameters vs. Arc Power and Deuterium Flow

Data presented in this section was measured using a radial probe located on axis. As previously mentioned, data points represent composite values obtained by averaging over multiple data sets. Saturated ion current density is defined by equation 48. No attempt has been made to relate data with theoretical predictions, due to their dependence on extensive numerical calculations.

Figure 22A and 22B plot plasma and arc parameters vs. arc power at an input deuterium flow of 6.5 T-ℓ/sec. For purposes of comparison, Figures 23A and 23B are electron probe current plots for arc power values of 4 kW and 53 kW respectively.

Figures 24A and 24B plot the same parameters vs. deuterium flow for fixed arc power of 22.6 kW. Gas flow values are accurate to within $\pm$ ½T-ℓ/sec for flow $\geq$ 4 T-ℓ/sec, and $\pm$ 1 T-ℓ/sec for flow $<$ 4 T-ℓ/sec. Figures 25A, 25B and 25C, illustrating the population enhancement of high energy electrons for low input gas flow, plots electron probe current characteristics for flows of 1, 6.5, and 17 T-ℓ/sec respectively.

ACKNOWLEDGEMENTS

My overall thanks to members of the LBL Neutral Beam Group for their general support and assistance. In particular, to: C. F. Burrell, J. R. Cary, C. F. Chan, W. S. Cooper, K. W. Ehlers and W. B. Kunkel for discussions on source physics; B. D. Billard for discussions and suggestions concerning the experimental apparatus W. F. Steele for computational assistance; E. B. Hewitt and D. J. Massoletti for maintaining test stand operation; and the shops of L. A. Biagi and H. A. Hughes. This work was performed under the auspices of the U. S. Department of Energy.

REFERENCES

1. K. W. Ehlers, W. R. Baker, K. H. Berkner, W. S. Cooper, W. B. Kunkel, R. V. Pyle, and J. W. Stearns, J. Vac. Sci. Technol. 10 (1973), 922-925.
2. J. G. Laframboise, U.T.I.A.S. R-100 (1966).
3. L. B. Loeb, "Basic Processes of Gaseous Electronics," University of California Press (1960), 329-373.
4. L. Schott, "Electrical Probes," in Plasma Diagnostics (Lochte-Holtgreven, eds.), North-Holland, Amsterdam (1968), 668-731.
5. Yu. M. Kagan and V. I. Perel, Soviet Phys. Usp. 6 (1964), 767.
6. B. M. Oliver, R. M. Clements and P. R. Smy, J. Appl. Phys. 44 (1973), 4511.
7. L. D. Landau and E. M. Lifshitz, "The Generalized Susceptibility" in Statistical Physics, Pergamon, New York, (1976)
8. P. M. Chung, L. Talbot and K. H. Touryan, "Electric Probes in Stationary and Flowing Plasma," Springer-Verlag, New York, (1975).
9. F. F. Chen, "Electric Probes," in Plasma Diagnostic Techniques (R. H. Huddlestone and S. L. Leonard, eds.), Academic Press, New York, (1965), 191-194.
10. R. L. F. Boyd and N. D. Twiddy, Proc. Roy. Soc. A 250 (1959), 53.
11. R. O. Lane, N. F. Morehouse Jr., and D. L. Phillips, Nuclear Instruments and Methods 9 (1960), 87-91.
12. B. R. Hunt, IEEE Transactions on Computers, Vol. C-22 9 (1973), 805-812.
13. I. Langmuir, Phys. Rev. 26 (1925), 585.
14. I. Langmuir and H. M. Mott-Smith, Phys. Rev. 28 (1926), 727.

15. D. Gabor, E. A. Ash, and D. Dracott, Nature 176 (1955), 916.

16. S. W. Rayment and N. D. Twiddy, Proc. Roy. Soc. A340 (1968), 87-98.

17. J. R. Cary, LBL-6365, (1977).

18. Barkhausen and Kurz, Phys. Zeits. 21, (1920), 1.

19. I. Langmuir and L. Tonks, Phys. Rev. 34 (1929), 876.

20. S. A. Self, Phys. Fluids 6 (1963), 1762.

21. S. A. Self, J. Appl. Phys. 36 (1965), 456.

22. G. S. Kino and E. K. Shaw, Phys. Fluids 9 (1966), 587.

23. E. K. Shaw, Ph.D. Thesis, Stanford University, (1967).

24. K. F. Schoenberg, C. F. Burrell, and W. S. Cooper, Bull. Am. Phys. Soc. 21 (1976), 1136.

25. W. S. Cooper, K. Halbach, and S. B. Magyary, LBL-3317 (1974).

26. C. F. Barnett, J. A. Ray, E. Ricci, M. I. Wilker, E. W. McDaniel, E. W. Thomas and H. B. Gilbody, Atomic Data for Controlled Fusion Research, ONRL-5206, (1977).

27. C. F. Chan, Private Communication.

28. L. Bromberg, Ph.D. Thesis, M.I.T. (1977).

FIGURE CAPTIONS

Figure 1A. Schematic cross section of the LBL 10 ampere neutral beam ion source.

Figure 1B. The 10 ampere source.

Figure 2. A typical probe voltage-current characteristic.

Figure 3. Experimental Apparatus.

Figure 4. Averaged plasma noise power density.

Figure 5. Probe driver-detection schematic.

Figure 6A. Differentiation network block diagram.

Figure 6B. Differentiation stage with compensation.

Figure 7. Probe/driver equivalent circuit.

Figure 8. $\omega_c/\pi \text{sinc}\left[\omega_c(t-\tau)\right]$.

Figure 9. Shadowed cavity cylindrical probe.

Figure 10. 2nd harmonic detection network.

Figure 11A. Driving signal network.

Figure 11B. Frequency doubling network.

Figure 12. Harmonic transfer function $\kappa(V_\phi^o, \varepsilon)$.

Figure 13A. Cylindrical probe characteristic.

Figure 13B. 1st derivative of probe characteristic.

Figure 13C. 2nd derivative of probe characteristic.

Figure 14A. Electron probability distribution function $f_e(\varepsilon)$.

Figure 14B. Total electron energy distribution function $F_e(\varepsilon)$.

Figure 14C. Computer plot of the electron probe current characteristic.

Figure 14D. Computer plot of the 1st derivative of the electron probe current characteristic.

Figure 15. Comparison of electron distribution function measurements using pulsed probe and harmonic analysis techniques.

Figure 16A. Electron energy distribution function - high energy tail: source center.

Figure 16B. Electron energy distribution function - high energy tail: source edge near filaments.

Figure 17. High energy electron probe characteristic.

Figure 18. Projected electron distribution function $f_e(\varepsilon,\hat{z})$: wall probe measurement.

Figure 19. Spatial probe diagnostics schematic.

Figure 20A. Radial plasma profile: Arc power = 16.3 kW
D_2 flow = 6T-ℓ/sec

Figure 20B. Radial plasma profile: Arc power = 21.6 kW
D_2 flow = 6T-ℓ/sec

Figure 21A. Axial plasma profile: Arc power = 16.3kW
D_2 flow = 6T-ℓ/sec

Figure 21B. Axial probe characteristic near source front for an arc power of 16.3 kW and deuterium flow = 6T-ℓ/sec.

Figure 21C. Axial probe characteristic near source rear for an arc power of 16.3kW and deuterium flow = 6T-ℓ/sec.

Figure 22A. Plasma potential, arc voltage, and arc current vs. arc power for on axis radial probe and deuterium flow = 6.5T-ℓ/sec.

Figure 22B. Bulk electron temperature, plasma density, and saturated ion current density vs. arc power for on axis radial probe and deuterium flow = 6.5T-ℓ/sec.

Figure 23. Electron probe current characteristic for on axis radial probe and deuterium flow = 6.5 T-ℓ/sec.

A. Arc Power = 4 kW.

B. Arc Power = 53 kW.

Figure 24A. Plasma potential, arc voltage, and arc current vs. deuterium flow for on axis radial probe and arc power = 22.6 kW.

Figure 24B. Bulk electron temperature, plasma density, and saturated ion current density vs. deuterium flow for on axis radial probe and arc power = 22.6 kW.

Figure 25. Electron probe current characteristic for on axis radial probe and arc power = 22.6 kW.

A. D_2 flow = 1 T-ℓ/sec.

B. D_2 flow = 6.5 T-ℓ/sec.

C. D_2 flow = 17 T-ℓ/sec.

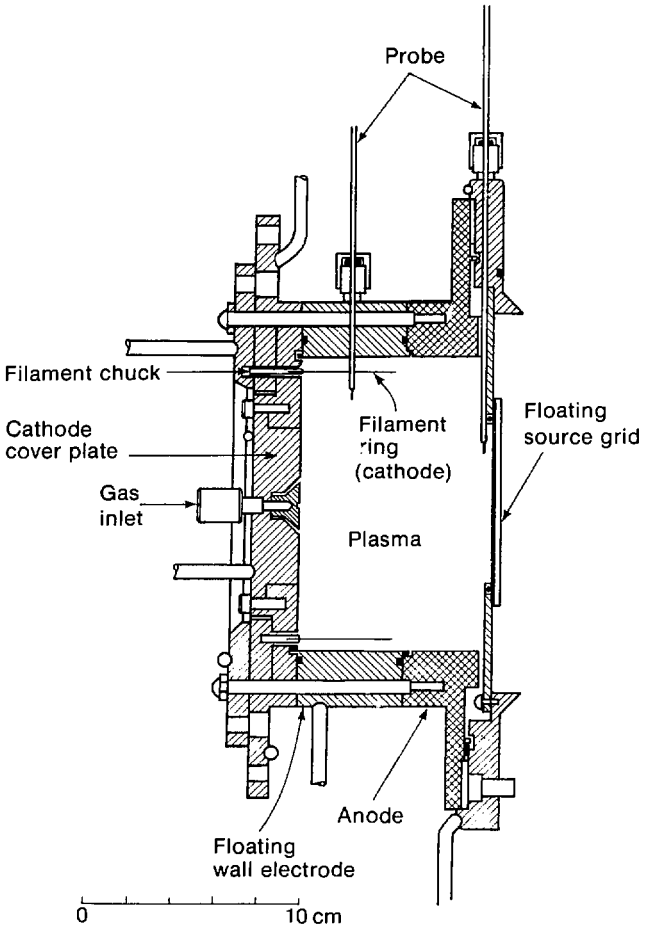

XBL 782-279

Figure 1A.

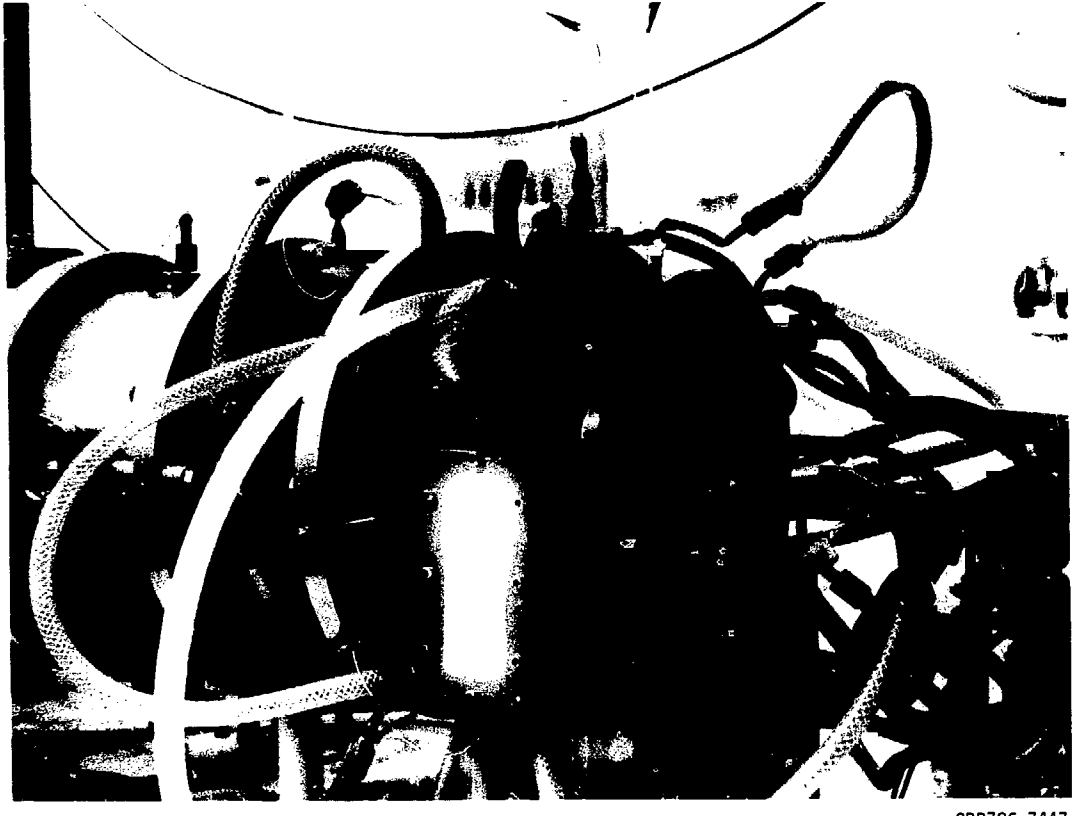

CBB786-7447

Fig. 1B

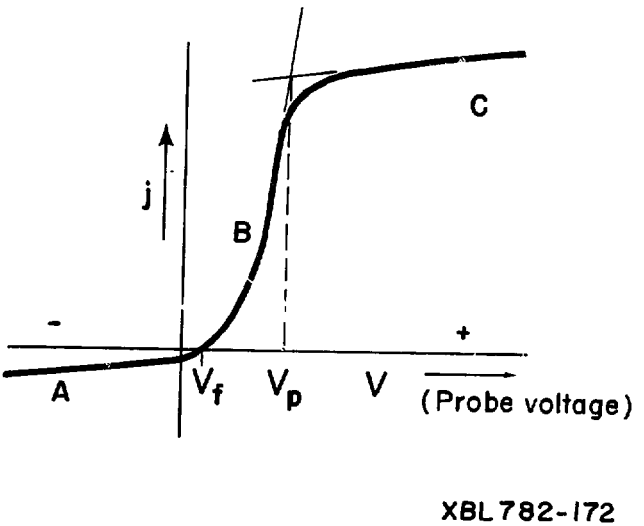

Figure 2.

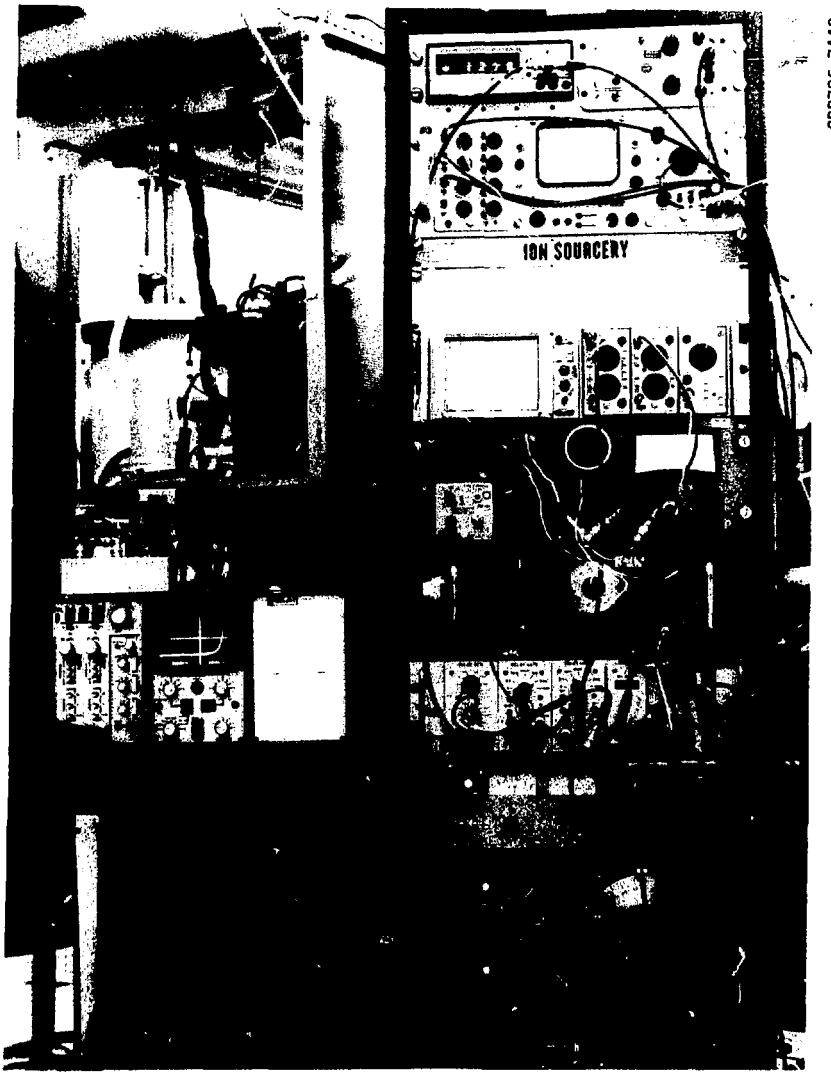

CBB786 7443

Fig. 3

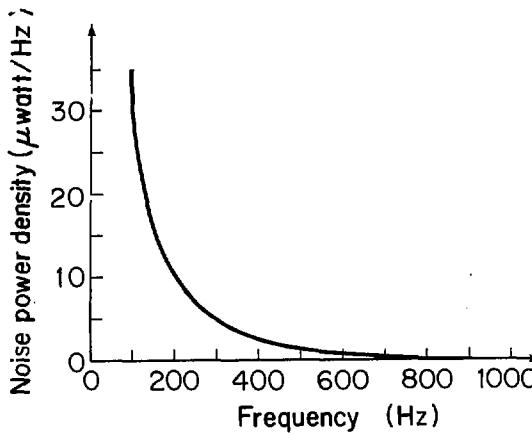

Figure 4.

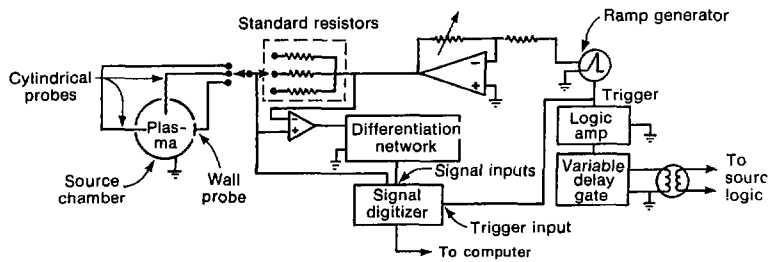

Figure 5.

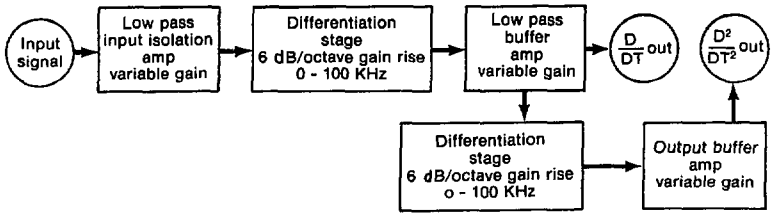

Figure 6A.

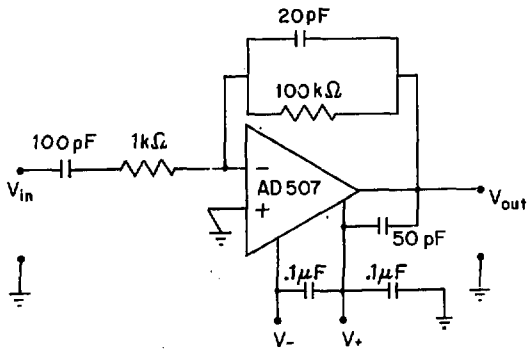

XBL 782-282A

Figure 6B.

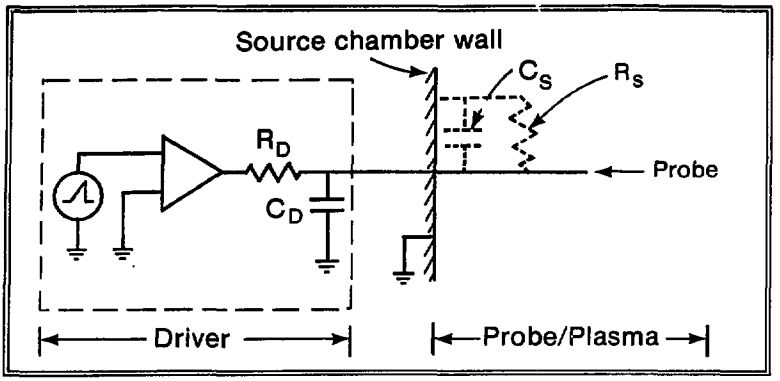

Figure 7.

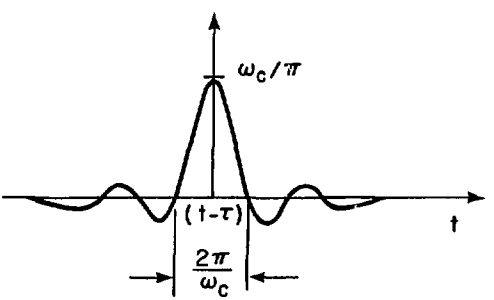

Figure 8. XBL 782-280A

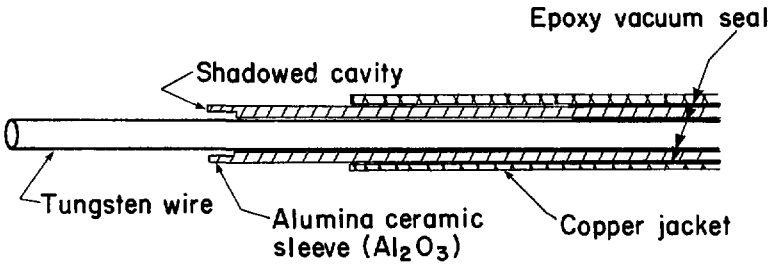

XBL 785-878

Figure 9.

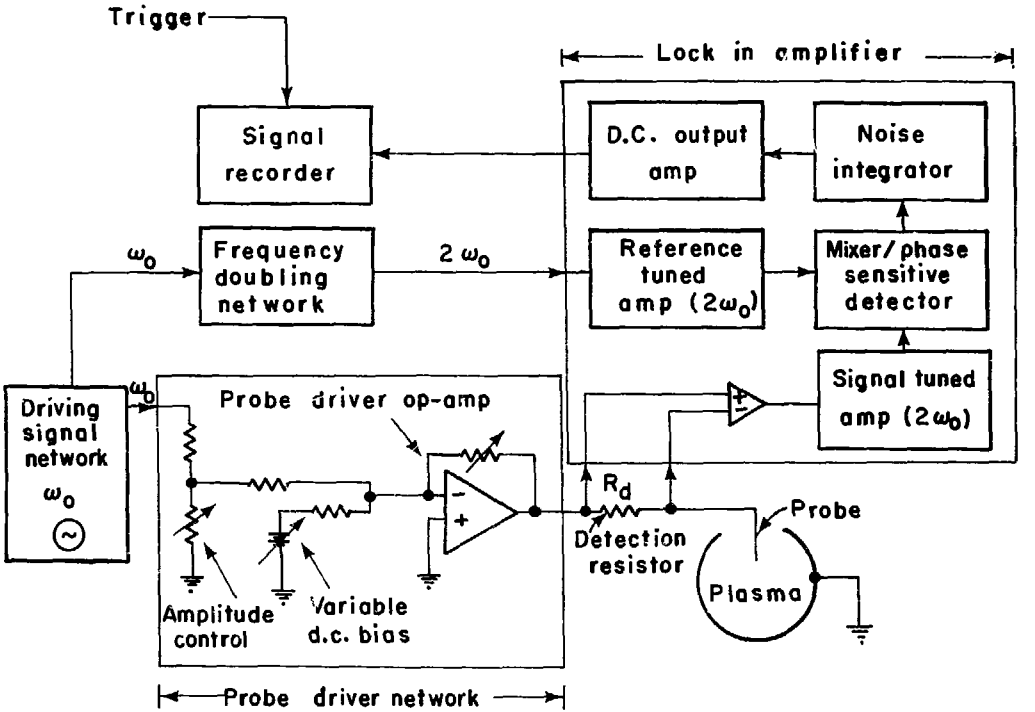

XBL786-1153

Figure 10.

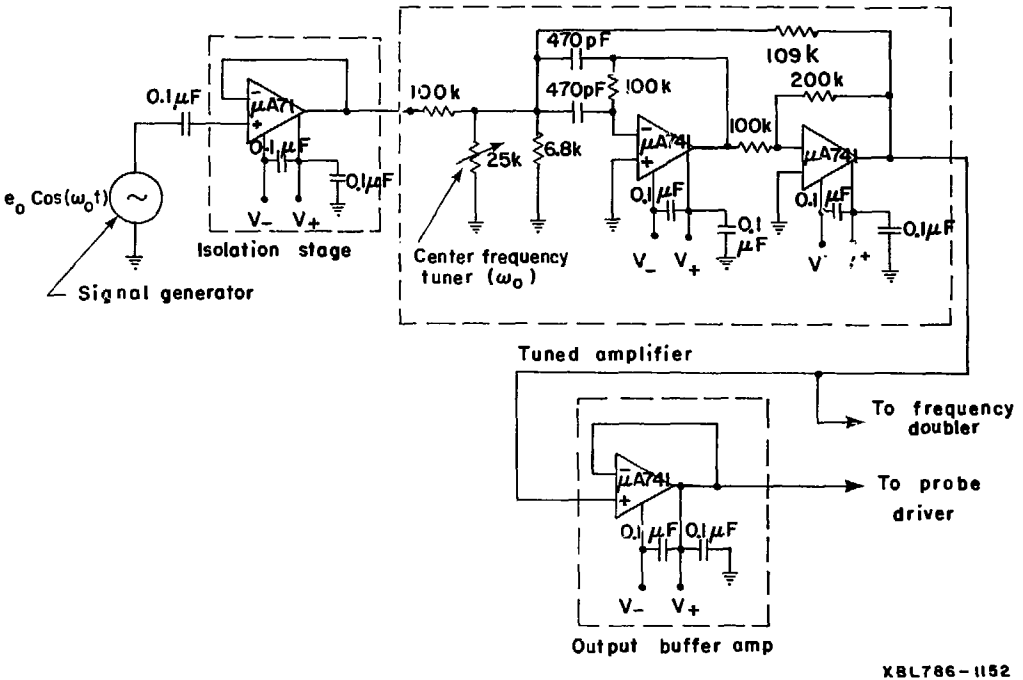
0.1μF
μA741
0.1μF
0.1μF
V- V+
Isolation stage
e0 Cos(ω0t)
Signal generator
100k
470pF
470pF
100k
25k
6.8k
Center frequency tuner (ω0)
μA741
0.1 μF
V- V+
0.1 μF
100k
109k
200k
μA741
0.1 μF
0.1μF
Tuned amplifier
To frequency doubler
To probe driver
μA741
0.1 μF
0.1μF
V- V+
Output buffer amp
XBL786-1152

Figure 11A.

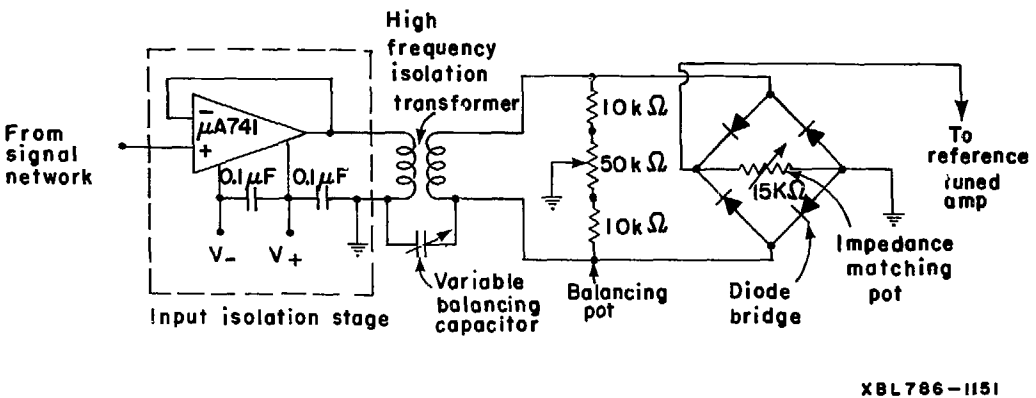
From signal network
μA741
0.1μF
0.1μF
V-
V+
Input isolation stage
High frequency isolation transformer
Variable balancing capacitor
10kΩ
50kΩ
10kΩ
Balancing pot
15KΩ
Diode bridge
Impedance matching pot
To reference tuned amp
XBL786-1151

Figure 11B.

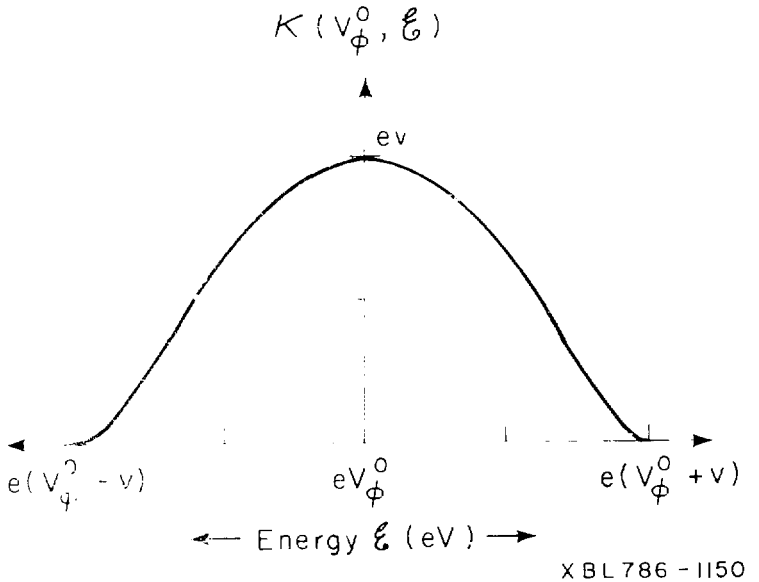
K (V$_\phi^o$, $\mathcal{E}$)
ev
e(V$_\phi^o$ - v)
eV$_\phi^o$
e(V$_\phi^o$ + v)
Energy $\mathcal{E}$ (eV)
XBL 786 - 1150

Figure 11.

A.

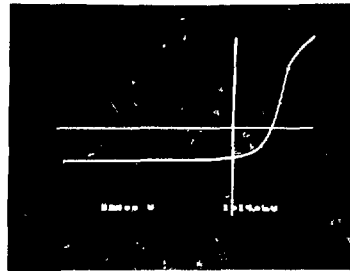

B.

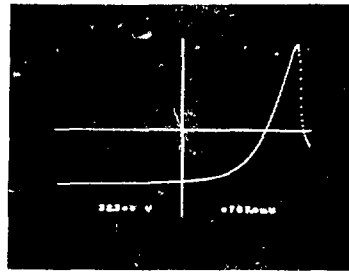

C.

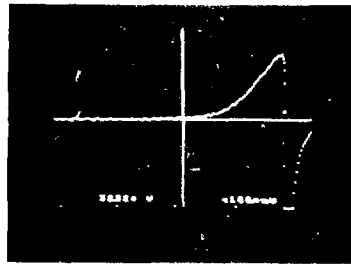

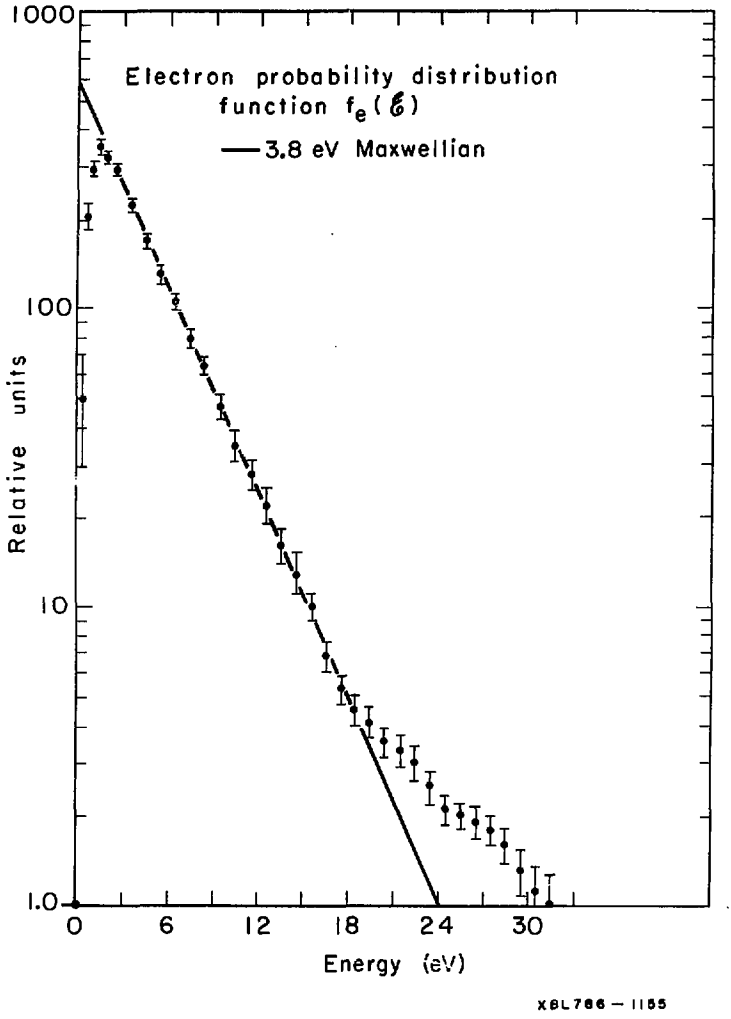
Electron probability distribution
function $f_e(\mathcal{E})$
—3.8 eV Maxwellian
1000
100
10
1.0
Relative units
0
6
12
18
24
30
Energy (eV)
XBL766—1155

Figure 14A.

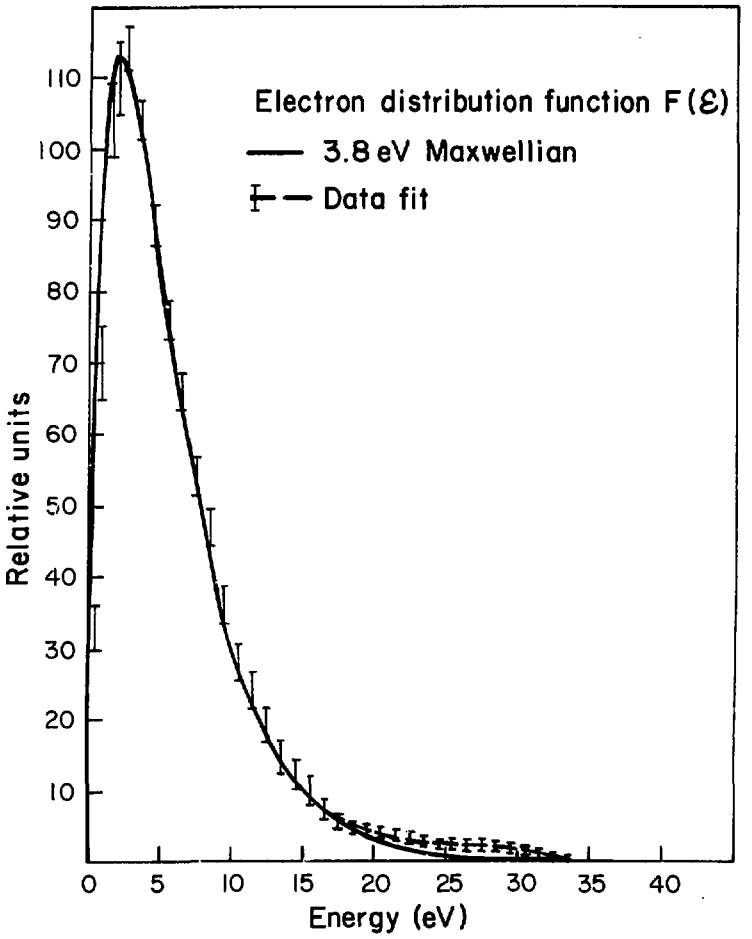

XBL 785-879

Figure 14B.

Arc Power: 16.3 kW Gas Flow: 6.5 T-ℓ/sec Source Center

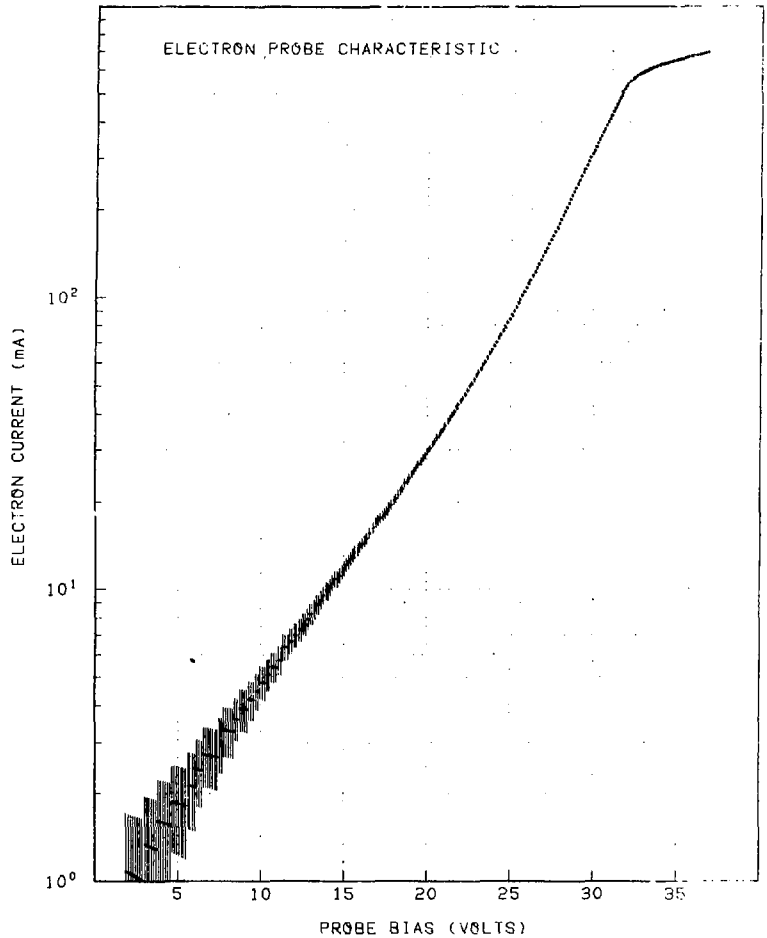

XBL 785-8672 A

Bulk Electron Temperature: 3.2 ± 0.2 eV
Electron Density: $2.0 \pm 0.3 \cdot 10^{12}$ /cm^3
Ion Density: $1.9 \pm 0.2 \cdot 10^{12}$ /cm^3

Figure 14C.

Arc Power: 16.3 kW Gas Flow: 6.5 T-ℓ/sec Source Center

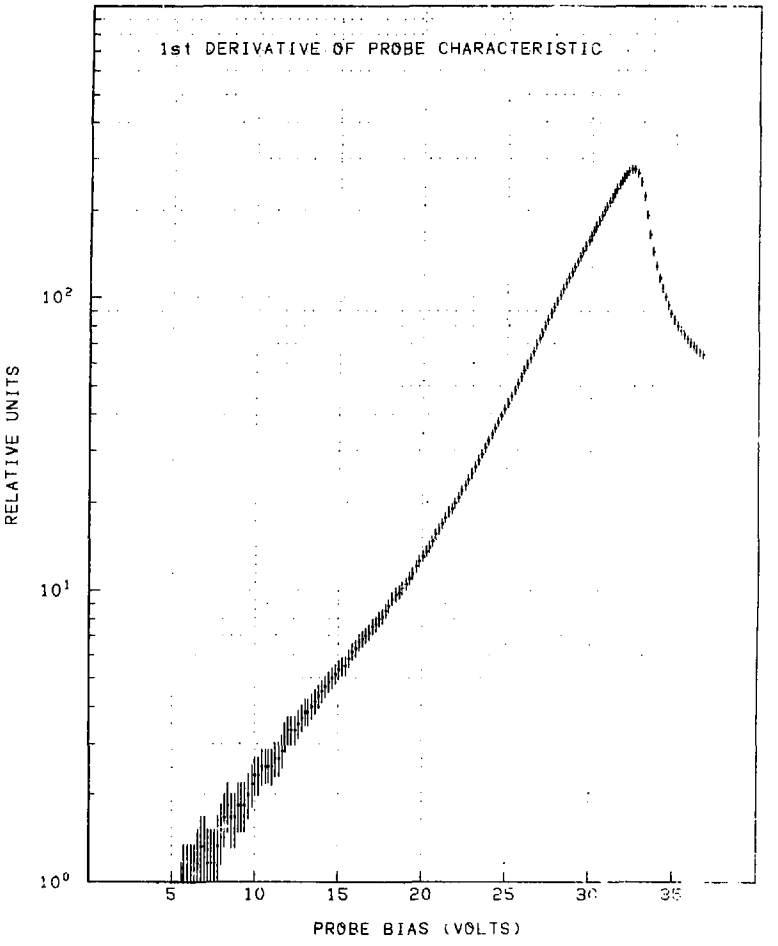

XBL 785 8599 A

Bulk Electron Temperature 3.8 eV

Figure 14D.

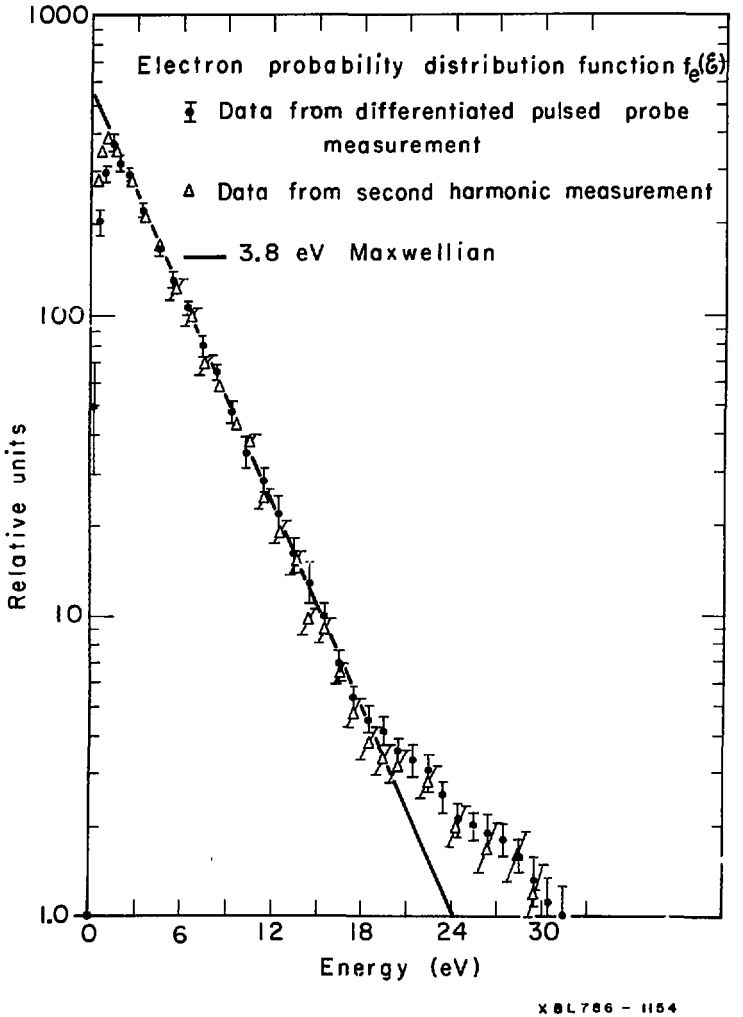
Electron probability distribution function $f_e(\mathcal{E})$
Data from differentiated pulsed probe measurement
Data from second harmonic measurement
3.8 eV Maxwellian
Relative units
1000
100
10
1.0
0
6
12
18
24
30
Energy (eV)
XBL786 - 1154

Figure 15.

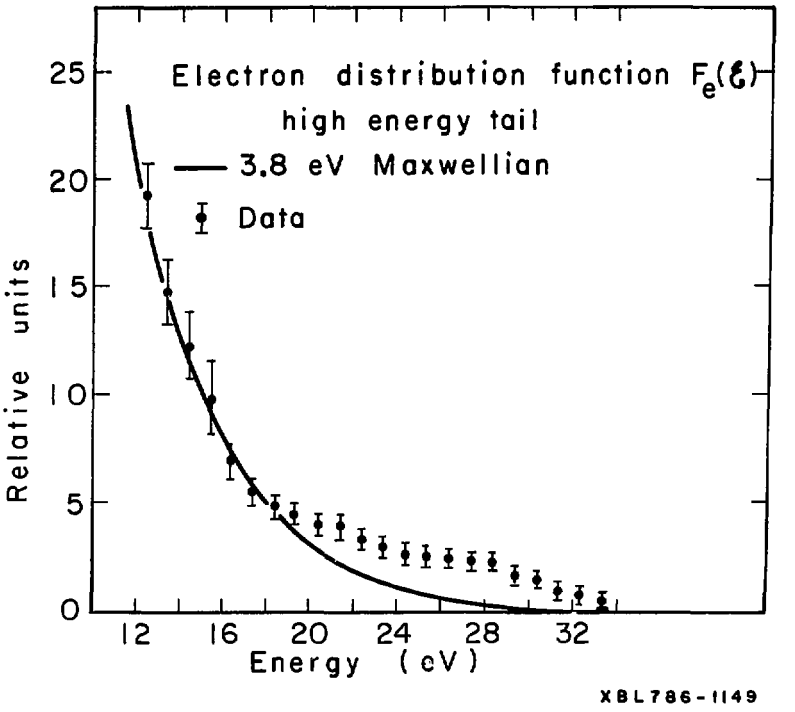
Electron distribution function $F_e(\mathcal{E})$
high energy tail
3.8 eV Maxwellian
Data
Relative units
25
20
15
10
5
0
12
16
20
24
28
32
Energy (eV)
XBL786-1149

Figure 16A.

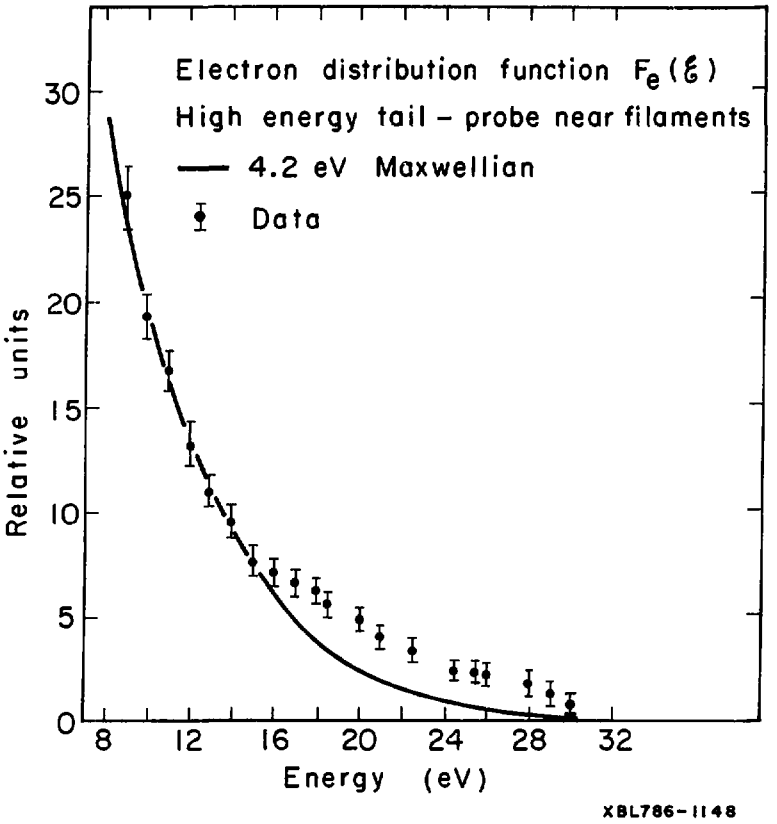
Electron distribution function $F_e(\mathcal{E})$
High energy tail – probe near filaments
4.2 eV Maxwellian
Data
Relative units
Energy (eV)
0
5
10
15
20
25
30
8
12
16
20
24
28
32
XBL786-1148

Figure 16B.

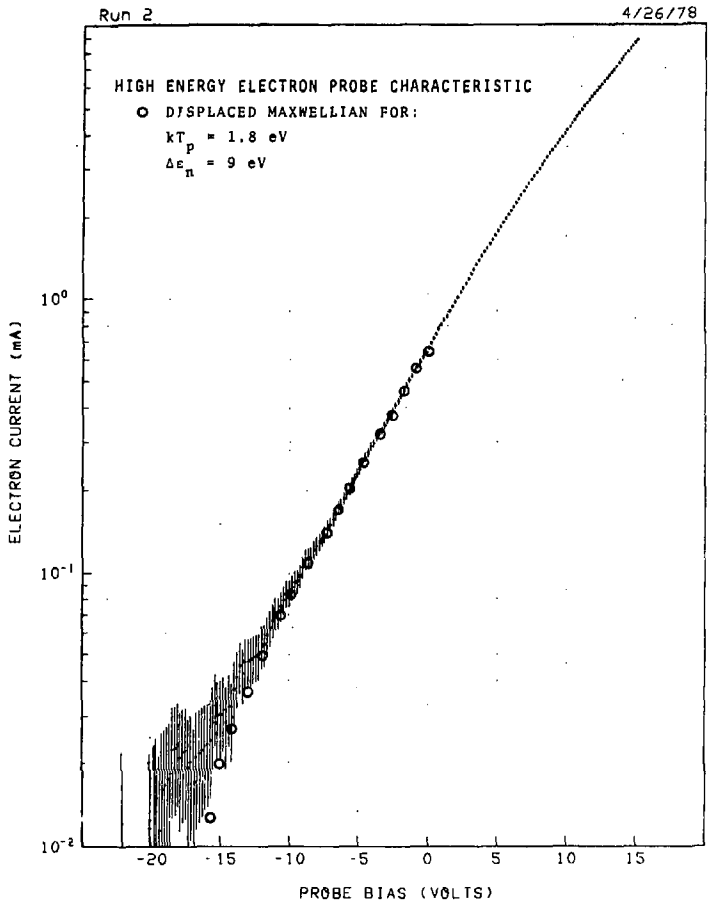

XBL 787-9588

Figure 17.

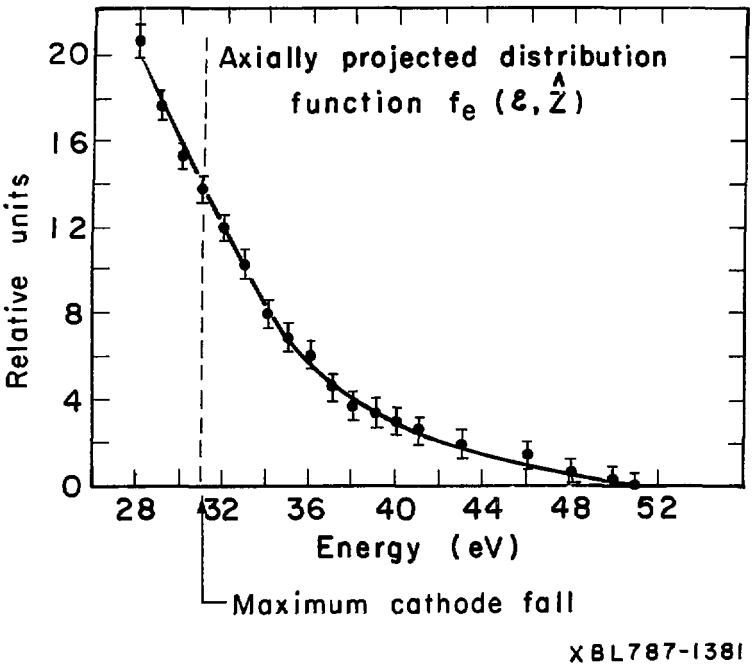
Axially projected distribution
function $f_e(\mathcal{E}, \hat{Z})$
Relative units
20
16
12
8
4
0
28
32
36
40
44
48
52
Energy (eV)
Maximum cathode fall
XBL787-1381

Figure 18.

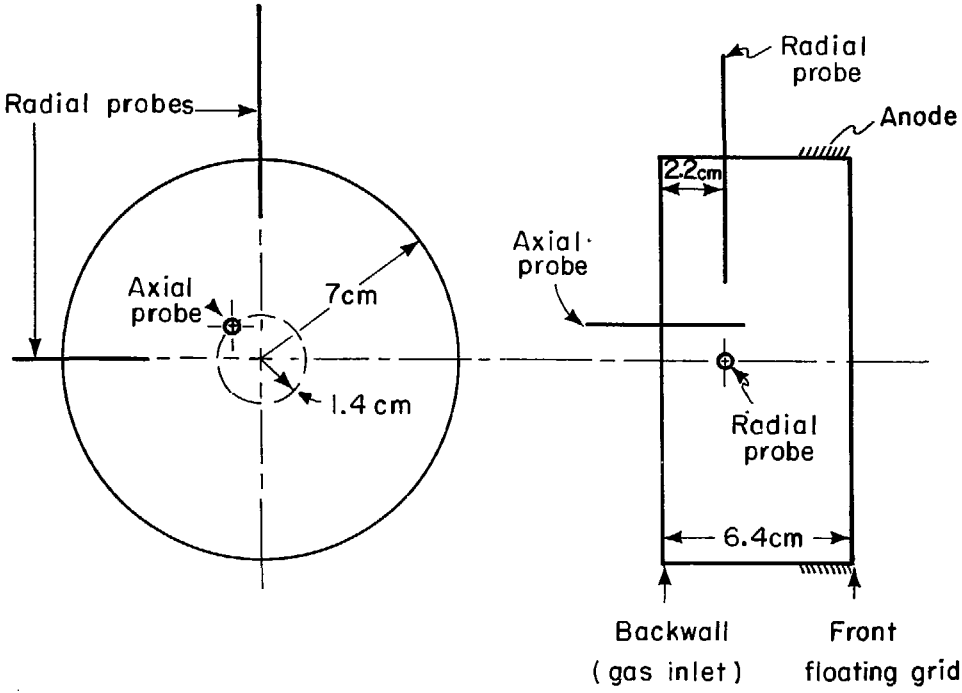

XBL787-1380

Figure 19.

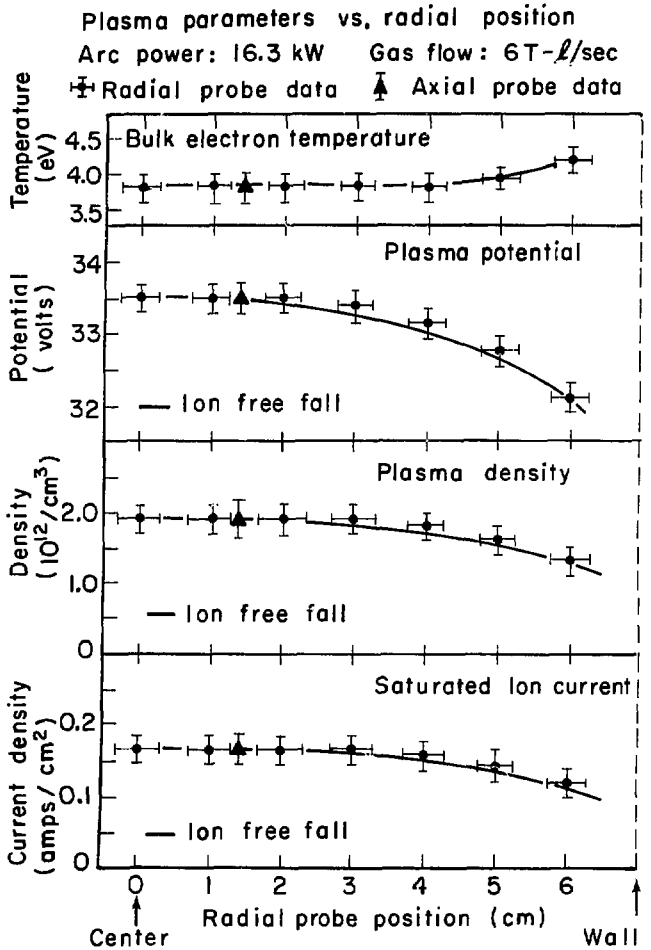

XBL787-1379

Figure 20A.

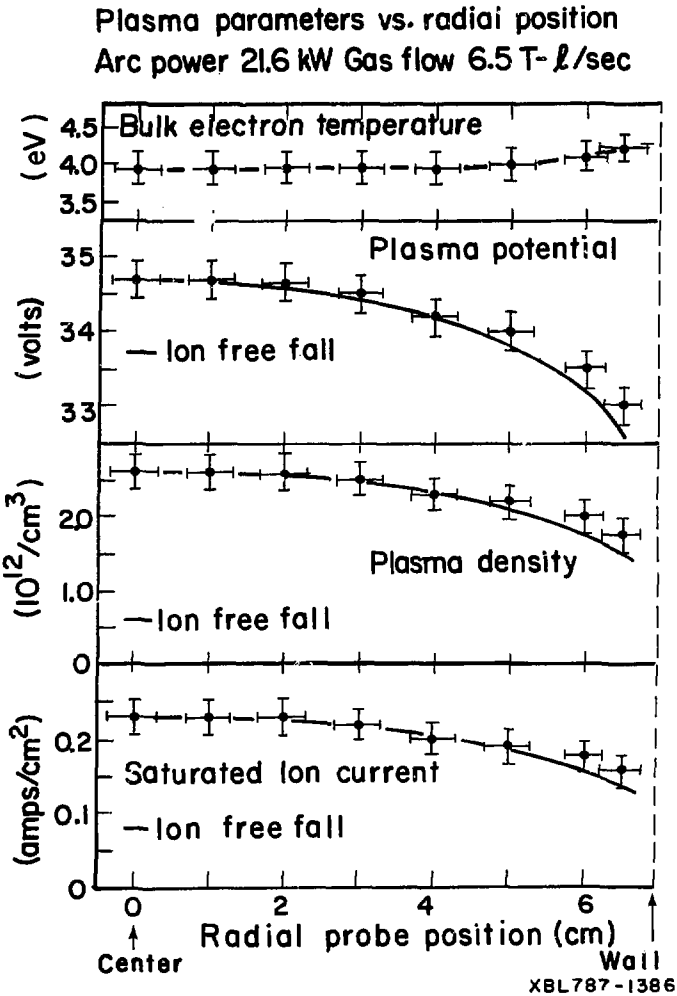
Plasma parameters vs. radial position
Arc power 21.6 kW Gas flow 6.5 T-ℓ/sec
Bulk electron temperature
(eV)
4.5
4.0
3.5
Plasma potential
35
34
33
(volts)
— Ion free fall
Plasma density
(10^12/cm^3)
2.0
1.0
0
—Ion free fall
Saturated Ion current
(amps/cm^2)
0.2
0.1
0
—Ion free fall
0
2
4
6
Radial probe position (cm)
Center
Wall
XBL787-1386

Figure 20B.

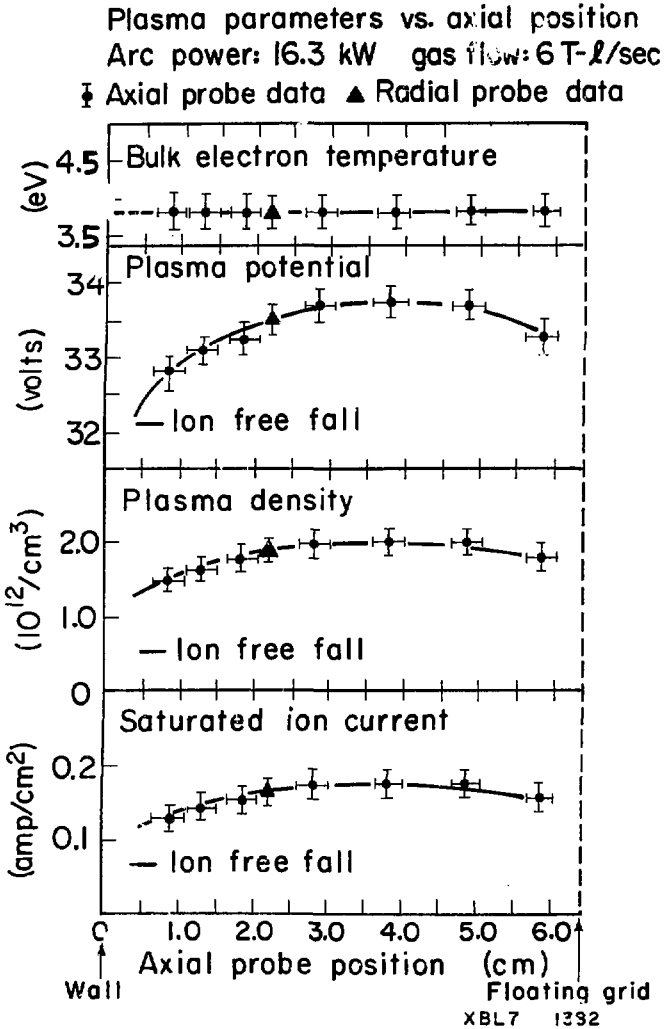
Plasma parameters vs. axial position
Arc power: 16.3 kW gas flow: 6 T-ℓ/sec
Axial probe data ▲ Radial probe data
Bulk electron temperature
(eV)
4.5
3.5
Plasma potential
(volts)
34
33
32
Ion free fall
Plasma density
(10^12/cm^3)
2.0
1.0
0
Ion free fall
Saturated ion current
(amp/cm^2)
0.2
0.1
Ion free fall
0
1.0
2.0
3.0
4.0
5.0
6.0
Axial probe position (cm)
Wall
Floating grid
XBL7 1392

Figure 21A.

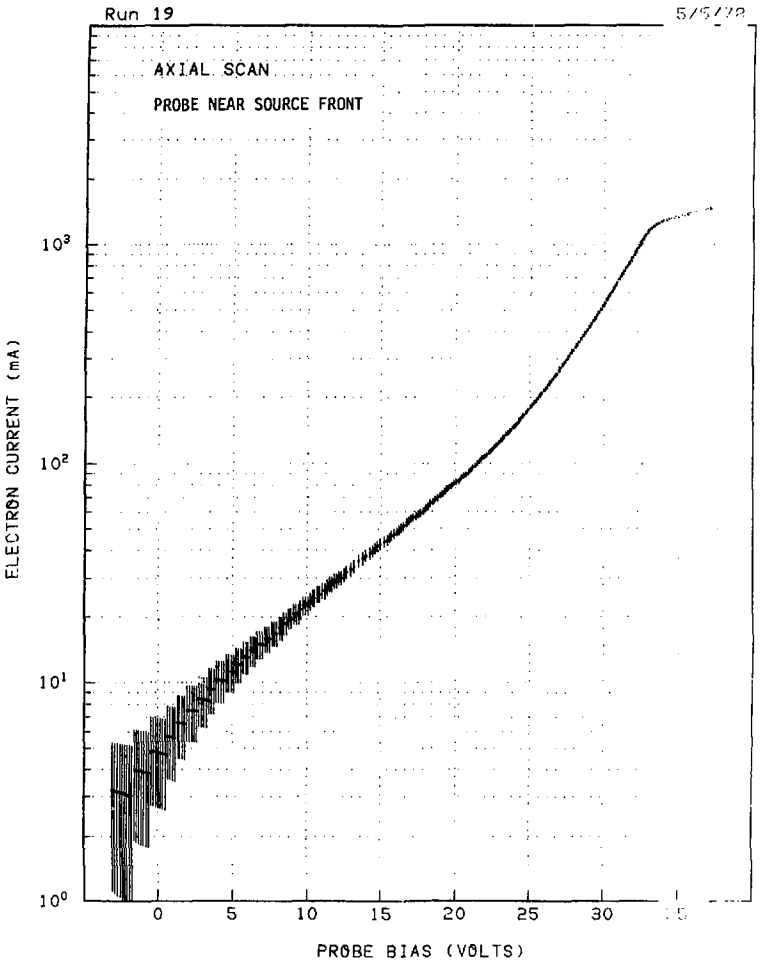

XBL 786-9333

Figure 21B.

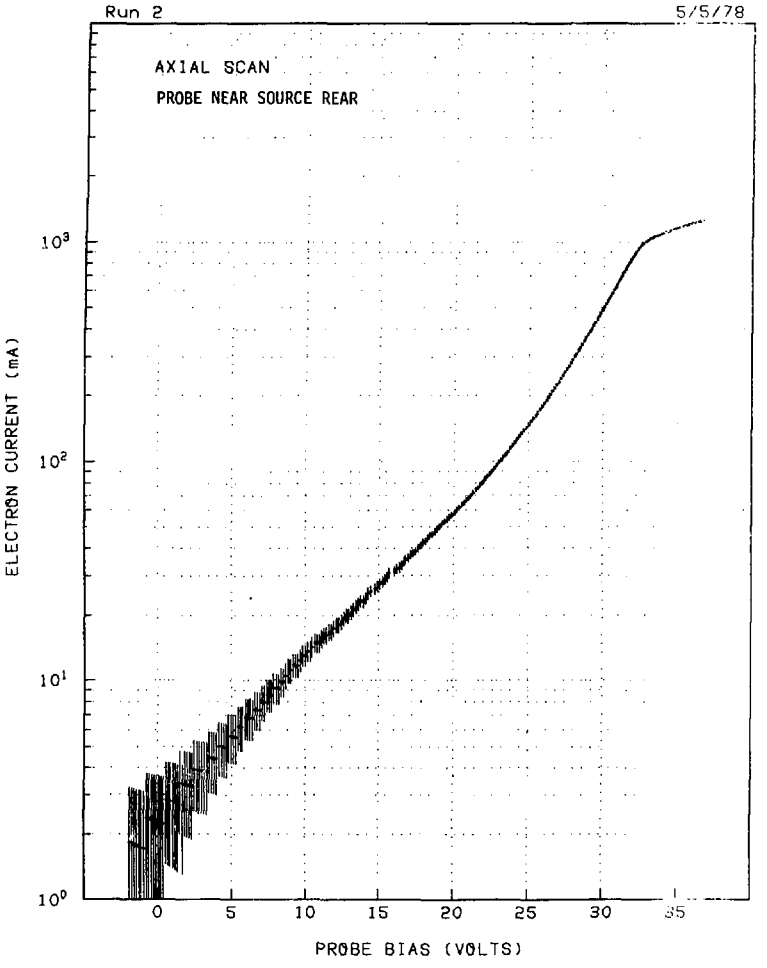

XBL 786-9332

Figure 21C.

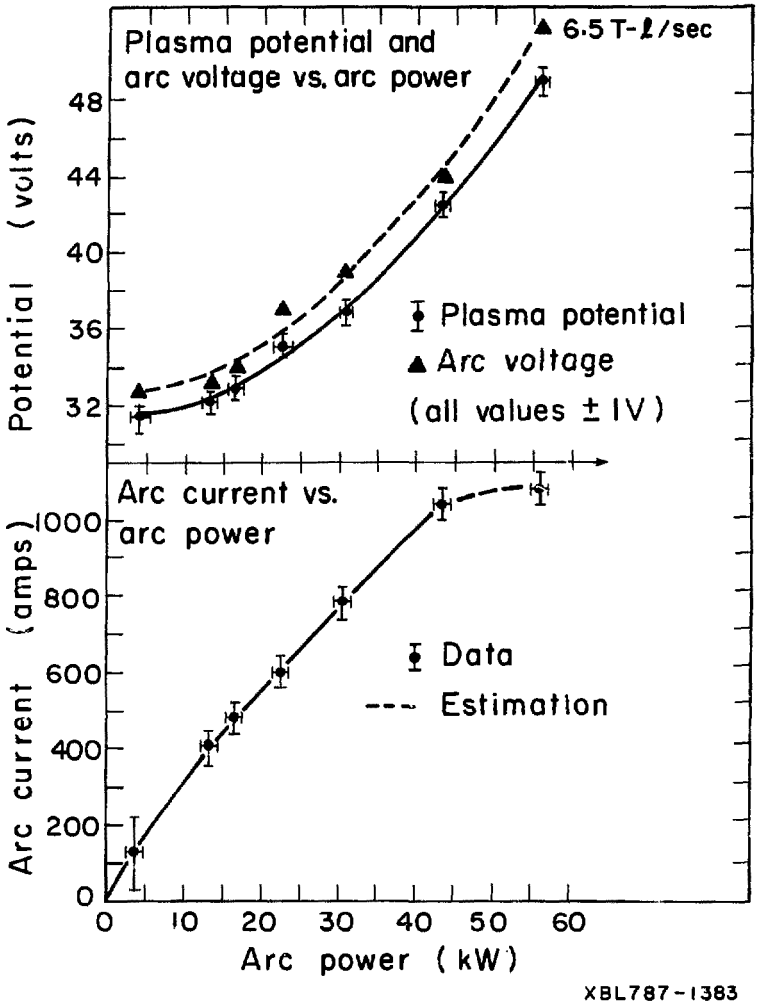
Plasma potential and
arc voltage vs. arc power
6.5 T-ℓ/sec
Potential (volts)
48
44
40
36
32
Plasma potential
Arc voltage
(all values ± 1V)
Arc current vs.
arc power
Arc current (amps)
1000
800
600
400
200
0
Data
Estimation
0
10
20
30
40
50
60
Arc power (kW)
XBL787-1383

Figure 22A.

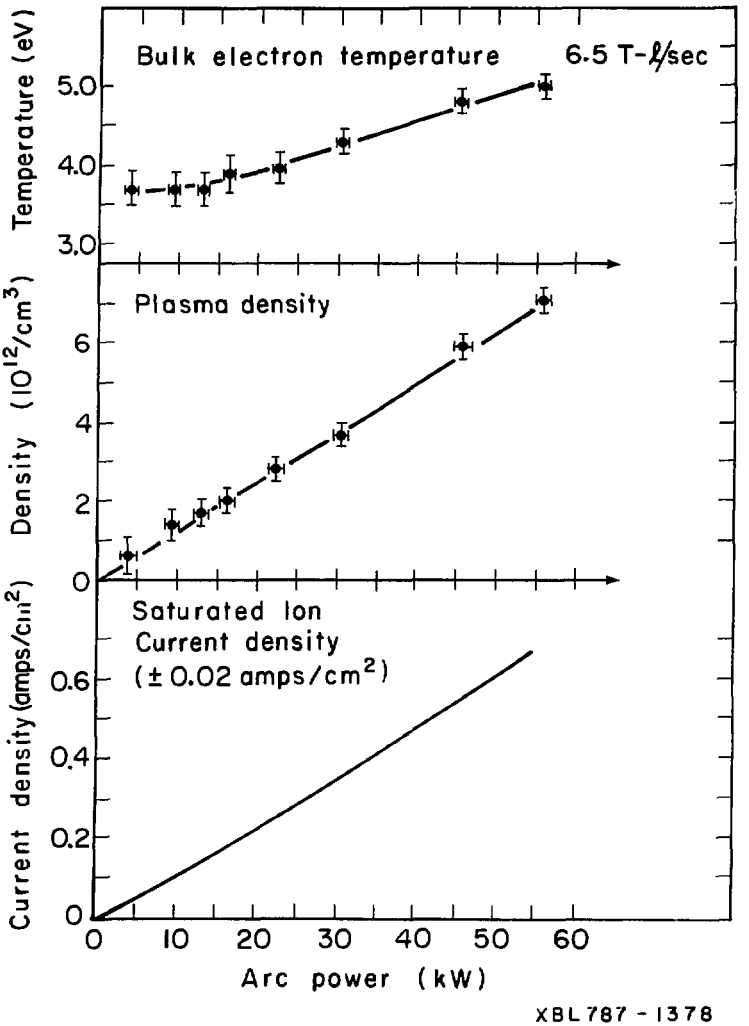
Bulk electron temperature
6.5 T-ℓ/sec
Temperature (eV)
5.0
4.0
3.0
Plasma density
Density (10^{12}/cm^3)
6
4
2
0
Saturated Ion
Current density
(± 0.02 amps/cm^2)
Current density (amps/cm^2)
0.6
0.4
0.2
0
0
10
20
30
40
50
60
Arc power (kW)
XBL 787 - 1378

Figure 22B.

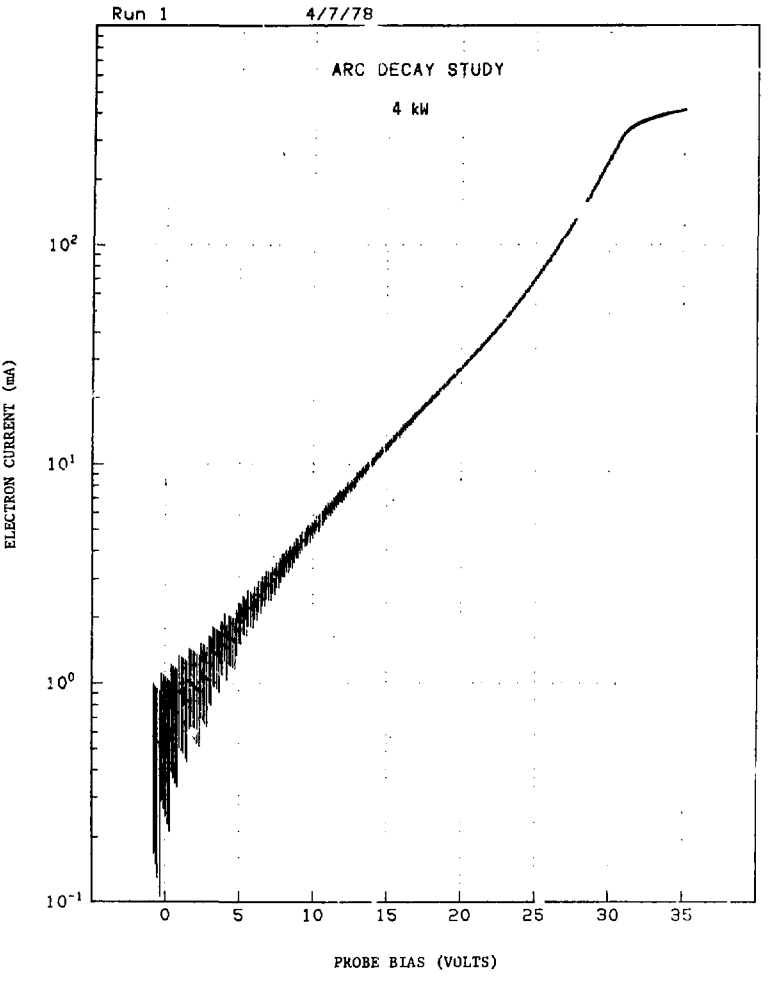

XBL 776-5335

Figure 23A.

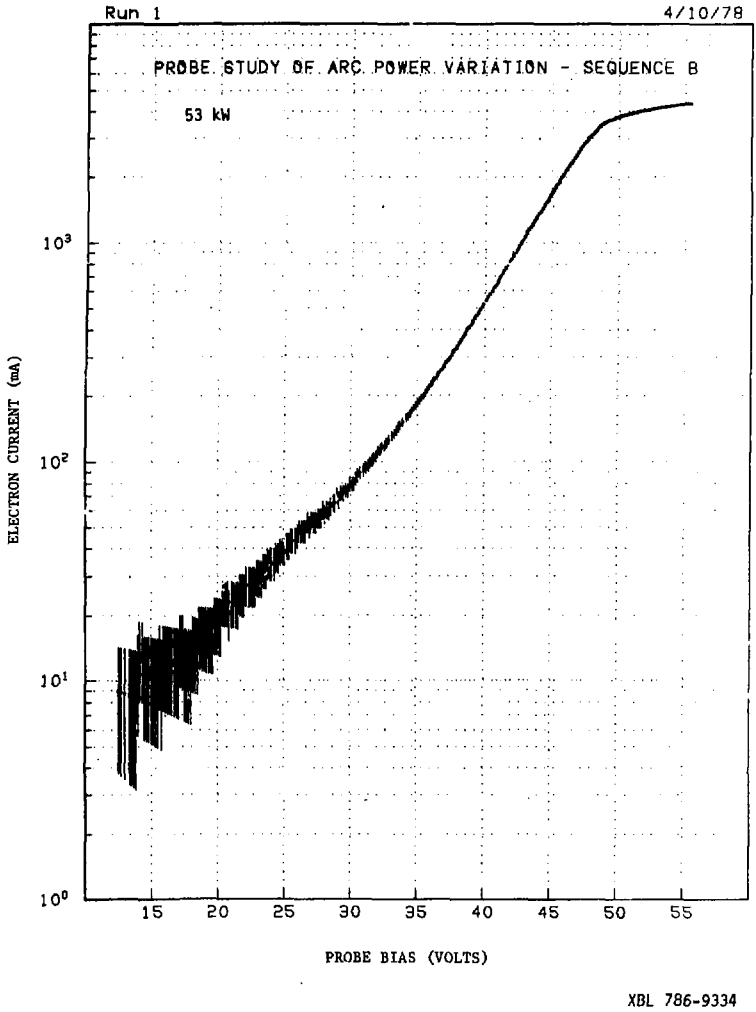
Run 1
4/10/78
PROBE STUDY OF ARC POWER VARIATION - SEQUENCE B
53 kW
ELECTRON CURRENT (mA)
10^3
10^2
10^1
10^0
15
20
25
30
35
40
45
50
55
PROBE BIAS (VOLTS)
XBL 786-9334

Figure 23B.

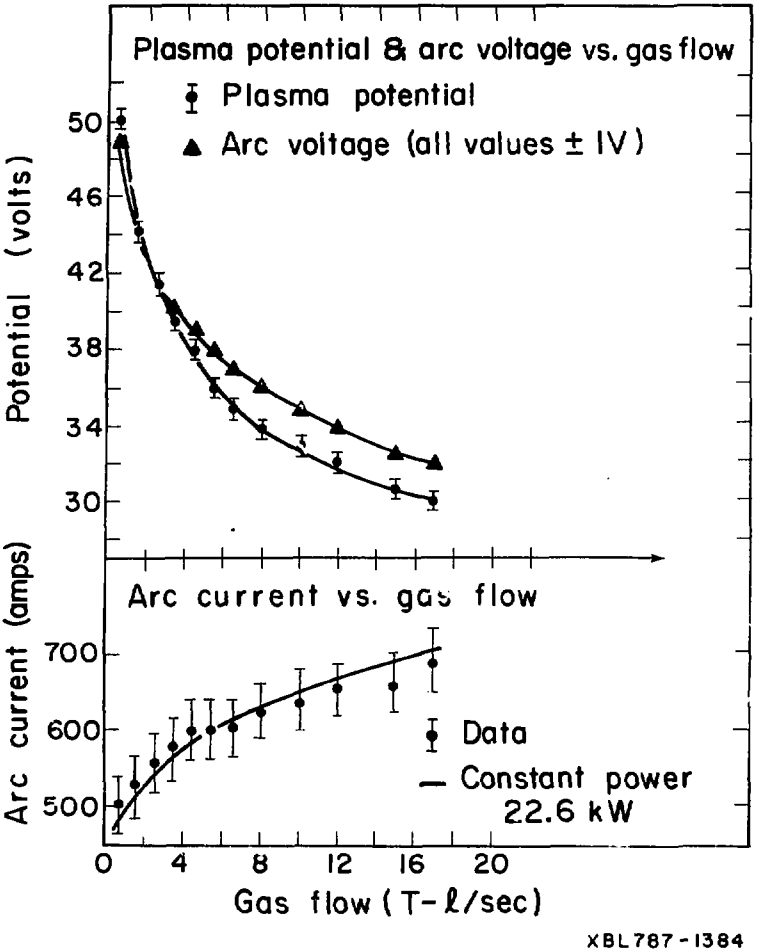
Plasma potential & arc voltage vs. gas flow
Plasma potential
Arc voltage (all values ± IV)
Potential (volts)
50
46
42
38
34
30
Arc current vs. gas flow
Arc current (amps)
700
600
500
Data
Constant power
22.6 kW
0
4
8
12
16
20
Gas flow (T-ℓ/sec)
XBL787-1384

Figure 24A.

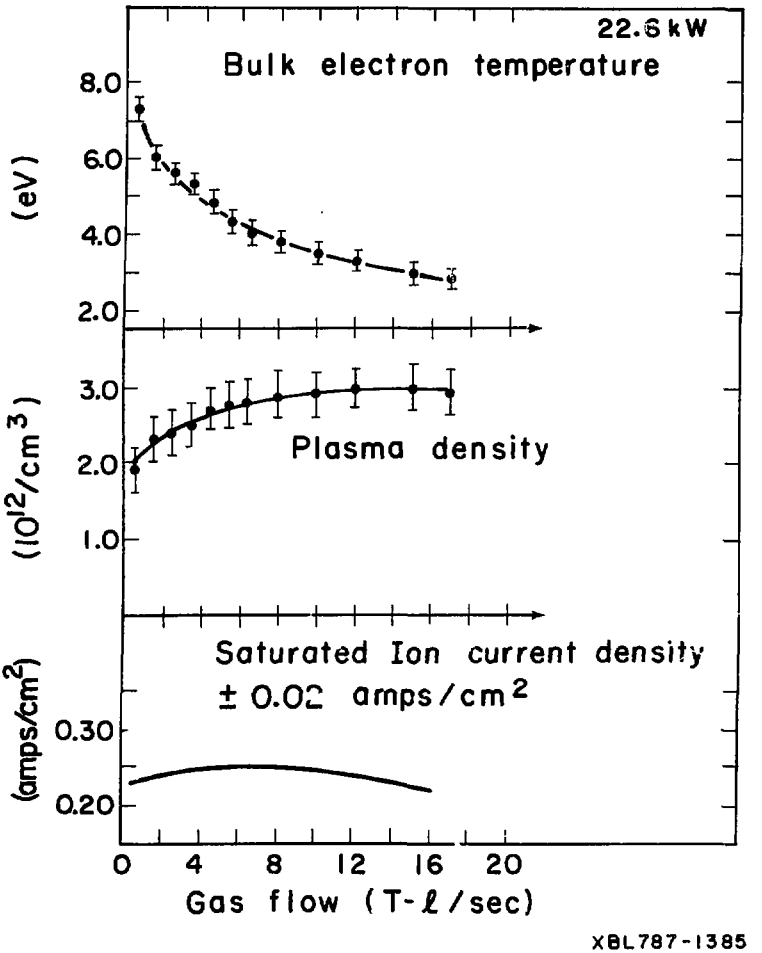
22.6 kW
Bulk electron temperature
8.0
6.0
4.0
2.0
(eV)
3.0
2.0
1.0
(10^12/cm^3)
Plasma density
Saturated Ion current density
± 0.02 amps/cm^2
0.30
0.20
(amps/cm^2)
0
4
8
12
16
20
Gas flow (T-ℓ/sec)
XBL787-1385

Figure 24B.

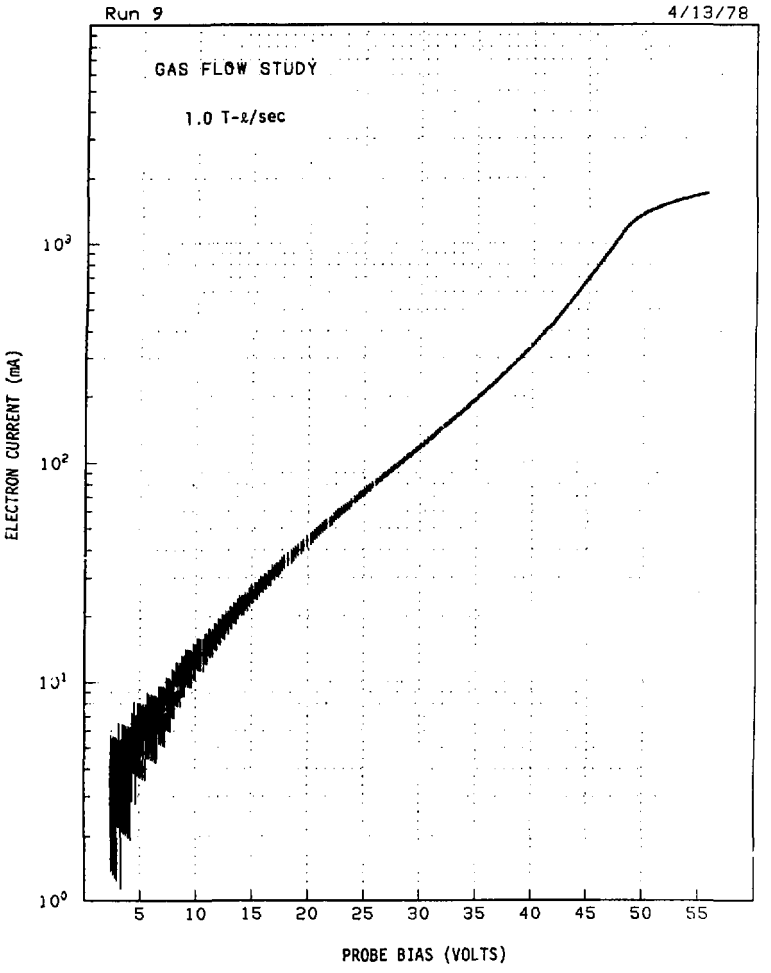

XBL 786-9245

Figure 25A.

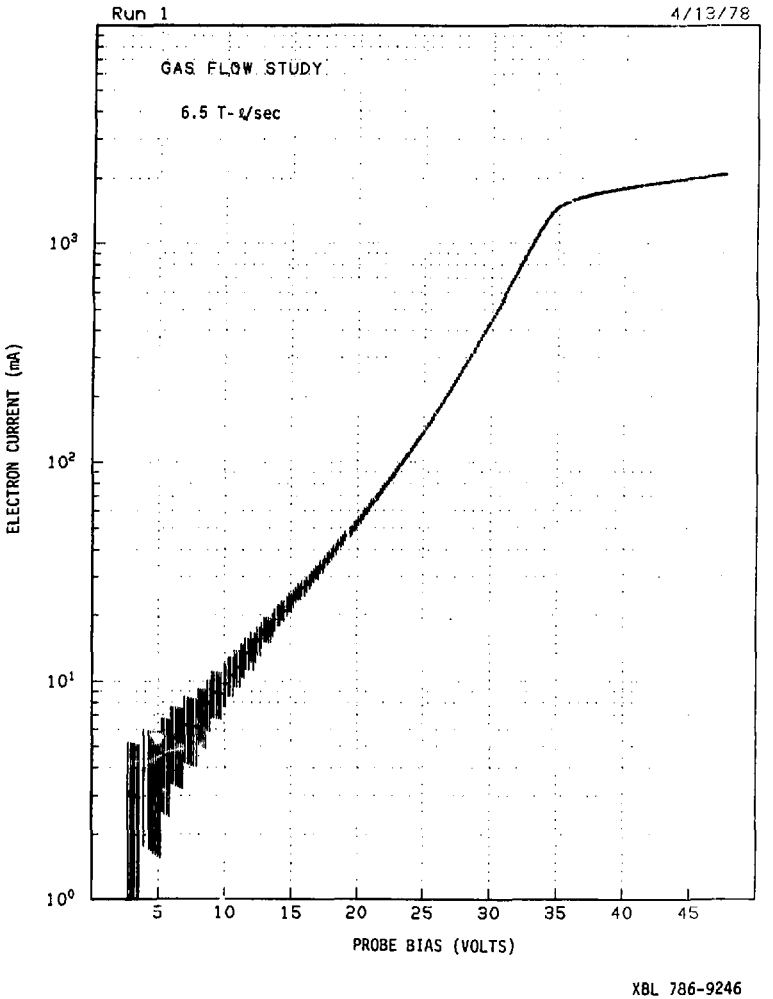
Run 1
4/13/78
GAS FLOW STUDY
6.5 T-ℓ/sec
ELECTRON CURRENT (mA)
10^3
10^2
10^1
10^0
5
10
15
20
25
30
35
40
45
PROBE BIAS (VOLTS)
XBL 786-9246

Figure 25B.

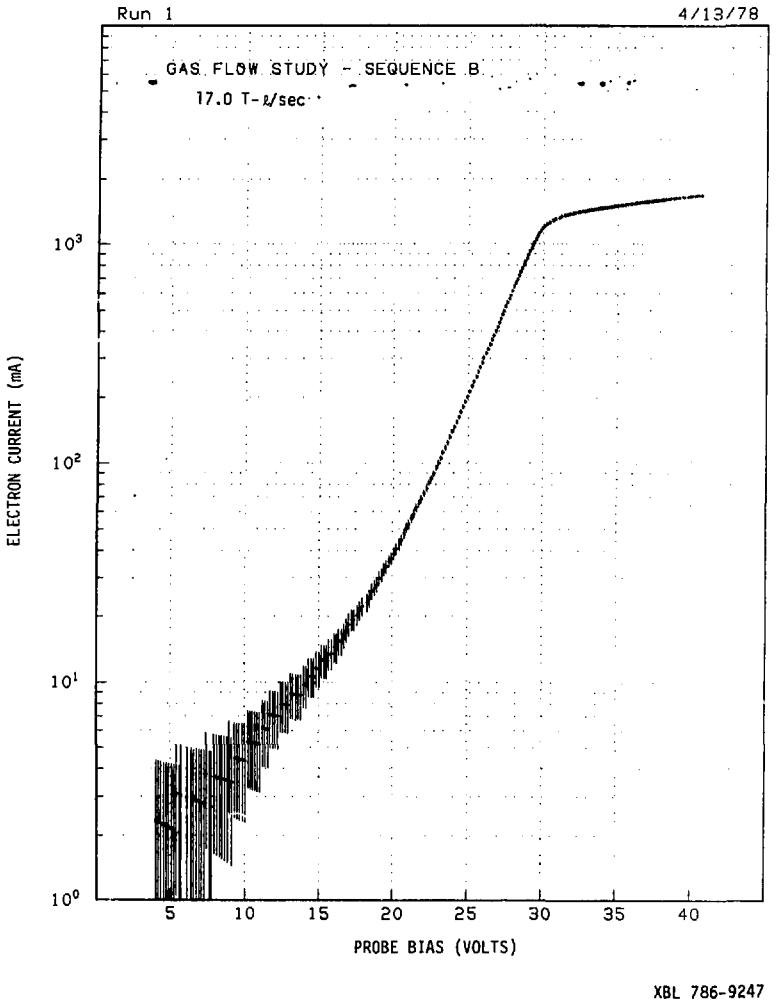
Run 1
4/13/78
GAS FLOW STUDY - SEQUENCE B
17.0 T-ℓ/sec
ELECTRON CURRENT (mA)
10^3
10^2
10^1
10^0
5
10
15
20
25
30
35
40
PROBE BIAS (VOLTS)
XBL 786-9247

Figure 25C.